



EUROPEAN ORGANIZATION FOR NUCLEAR RESEARCH

CERN-EP/87-87
May 7th, 1987

CHANNELING RADIATION FROM 2 TO 55 GeV/c ELECTRONS AND POSITRONS
II. AXIAL CASE

J.F.Bak, J.A.Ellison*, B.Marsh[†], F.E.Meyer,
O.Pedersen, J.B.B.Petersen, and E.Uggerhøj
Institute of Physics, University of Aarhus, Denmark

S.P.Møller and Allan H.Sørensen
CERN, Geneva, Switzerland

M.Suffert
Centre de Recherches Nucleaires, Strasbourg, France

(Submitted to Phys.Rev.B)

-
- * Visitor from Department of Mathematics and Statistics,
University of New Mexico, Albuquerque, N.M., USA
 - [†] Visitor from SUNY at Albany, Albany, N.Y., USA

Abstract

Radiation spectra for GeV electrons and positrons have been measured in a broad range of incidence angles in Si and Ge crystals. An enhancement up to a factor of 50 is found for axially channeled particles. In nearly all cases, the low-energy part of the photon spectra is strongly reduced either due to equalization in the doughnut or due to the strong multiple scattering from the atomic rows. For large incident angles to the axis, the reduction is due to the so-called Landau-Pomeranchuk effect. For proper channeled positrons, stable oscillations give rise to a peak in the photon spectra. In the transition region from axial to planar channeling, the photon spectra change from being structureless to showing pronounced peaks from the first harmonics. The experimental results are compared to both classical and quantal calculations.

I. Introduction

In the sixties, when coherent bremsstrahlung (CB) was discovered, most experimental work was performed with parallel electron beams in the low GeV region. Whenever the incident directions were close to axial/planar directions, pronounced peaks were found in the low-energy part of the photon spectra. These peaks were difficult to explain, however, from the theory of CB, (for a review of CB, see ref.1). In reality, many of the spectra were a mixing of CB and channeling radiation (CR) which was predicted ten years later. Since the mid-seventies, CR has been studied extensively both theoretically and experimentally from the MeV to the hundred-GeV region (for a review, see ref.2). These investigations have revived the interest for CB because CB and CR can be considered as two different but related aspects of the same physical phenomenon and can be described in a unified fashion.

For the planar cases, the overall understanding of CR is good, although some disagreement exists between measured and calculated photon energies emitted by MeV channeled positrons (for a review, see refs.2 and 3). A detailed discussion of planar radiation from 2- to 55-GeV/c electrons/positrons was presented in an earlier paper⁴ (hereafter referred to as I). Here it was stressed that our original disagreement between measured and calculated energies of first harmonics for positrons has been removed through detailed momentum measurements on the CERN beamline. Also some of the disagreements in other GeV experiments have been corrected⁵.

The understanding of photon spectra from axially channeled electrons/positrons is not complete, however. Theoretically, both classical and quantum mechanical calculations^{2,6,7,8} have been performed, but the two-dimensional nature of the axial case often makes the computations cumbersome. For MeV particles the so-called many beam calculations, as well as other quantum mechanical approaches give good agreement with experiments, especially for

electrons despite their negative charge^{2,3}. In the GeV region, such procedures become very complicated because of the many quantum states of transverse motion (~500), but here a classical approximation can be used as long as the quantum recoil during radiation is negligible (low photon energies)^{2,7,8}.

For large photon energies in the multiple-GeV region, however, the classical description of channeling radiation becomes invalid. The breakdown is clearly not due to lack of quantum states but associated with the quantum recoil during radiation. Now the photon energy amounts to an appreciable fraction of the primary energy and cannot be neglected as in a classical treatment.

At these high energies, the emission angle $1/\gamma$ is small compared to critical channeling angles $\psi_c \propto 1/\sqrt{\gamma}$. Therefore the emission to a good approximation can be considered as being due to the motion in a constant field. In this model, the radiation can be calculated in the synchrotron approximation^{2b} or using the quasiclassical operator method⁹.

Along with the radiation from purely axially channeled particles, there is a very enhanced radiation in the region of the so-called doughnut scattering, where particles are free to move in the transverse plane but scatter off rows of atoms - strings - as a whole^{10,11}. At GeV energies, this effect is observed for incident angles up to 15-20 times the Lindhard critical angle ψ_c .

Experimental investigations of the radiation from axially channeled particles have been performed by different groups (for a review, see refs. 2, 7, and 8). Most axial photon spectra are broad and structureless especially for the low-energy part. For the high-energy part, new and very interesting, though unresolved, effects have very recently been reported. Aganyants et al.¹² find axial yields below random for hard photons emitted by 4-GeV elec-

trons beyond the coherent part of the spectrum. Even more spectacular, Belkacem et al.¹³ find pronounced peaks at ~80% of the incidence energy in axial yields from 150-GeV electrons but smooth spectra for positrons. At such high energies, the coherent part of the radiation spectrum extends all the way to the incidence energy.

The present paper presents detailed experimental investigations of the low-energy part of the radiation spectra near the axial direction. Specific peaks are for the first time found for proper channeled particles. The transition region between axial- and planar-channeling radiation is investigated, together with the effect from doughnut scattering. Strong reductions in low-energy photon yields are found due to doughnut scattering in the dipole limit. Above the dipole region, a strong reduction is found due to the so-called Landau-Pomeranchuk effect. Also, the transition from the region of coherent bremsstrahlung to channeling radiation is discussed. Throughout, the presentation of data is accompanied by theoretical considerations, and comparisons are given to theoretical results.

II. Experimental Setup

A detailed description of the experimental setup together with a discussion of crucial parameters, e.g., drift velocity in drift chambers, angular resolution, detector resolutions, and target quality, can be found in I. Here, only a brief overview will be given.

The experiment was installed in the t_7 beam of the CERN 28-GeV/c proton synchrotron. This is a non-separated beam, containing mainly electrons/positrons, pions and protons, with a momentum adjustable between 2 and 10 GeV/c in positive and negative polarity. The positron content varied from 50% at 2 GeV/c to 0.5% at 10 GeV/c, whereas the electron content was somewhat larger, due to the very small content of antiprotons. The momentum spread was ad-

justable with momentum slits and was typically 1%. The beam divergence was ± 1 mrad, and the useful part of the beam had a size of 15 mm on the target. The beam intensity was around 10^5 sec^{-1} .

A schematic lay-out of the experiment is shown in fig.1. Scintillation counters SC1 and SC3 in anticoincidence with SC2 were used to define the useful part of the beam and supplied triggers for the data acquisition system. Drift chambers, denoted DC on the drawing, were used to track each particle passing through the setup. Vacuum tubes were placed between the drift chambers in order to eliminate multiple scattering and background radiation. The position resolution of the drift chambers was 0.1 mm. A distance of 15 m between the two first chambers results in an angular resolution of 20 μ rad of the incident beam. Particle identification was made with threshold Cerenkov counters, placed after DC-3, and a lead-glass array assured the e^+/e^- identification. The emitted radiation was detected with a 10"x12" NaI crystal. The energy resolution of this photon detector was 4% at 50 MeV, degrading to 8% at 5 MeV and 100 MeV.

The background-radiation level corresponds to the incoherent bremsstrahlung from 190 μ m amorphous silicon, mainly consisting of incoherent bremsstrahlung, produced as the particles passed through DC2 and the surrounding mylar windows. This radiation background was subtracted from the spectra presented in this paper.

Triggers for the data acquisition system were generated by all positrons (or electrons), giving a signal larger than 4 MeV in the NaI detector. Furthermore, a certain fraction of the total beam was recorded, so the spectra could be normalized. The information for each event was registered in pattern units, TDC's and ADC's in a CAMAC crate and stored on magtape for subsequent analysis on mainframe computers in Aarhus and at CERN. A small on-line computer supervised the data acquisition and analyzed samples of the

data.

III. Some Relevant Channeling and Radiation Concepts

III.1. Axial Channeling

As pointed out in I, the Bohr condition ($\kappa \approx 2Z_1 Z_2 / 137\beta \gg 1$) for a classical orbital description in a collision with a single atom is not fulfilled for high velocities v , where $\beta = v/c \sim 1$. In the transverse plane, however, where most of the channeling motion can be described, the Bohr condition turns into the Lindhard condition, i.e.,

$$\kappa_{\perp} = 2 \left[\frac{M}{m} Z_1 Z_2^{1/3} \frac{a_0}{d} \right]^{1/2} \gg 1 \quad (1)$$

where M is the relativistic particle mass and m the electron rest mass, a_0 the Bohr radius, and d the atomic spacing along the string. This condition is certainly fulfilled for GeV particles. Therefore classical relativistic mechanics will be used in the following. Also classical electrodynamics will be used as long as the quantum recoil is negligible during the emission of radiation.

The relativistic equations of motion for the axial continuum model are for electrons/positrons

$$\frac{d\gamma \vec{r}_{\perp}}{dt} = - \nabla_{\perp} U(\vec{r}_{\perp}) \quad (2)$$

$$\frac{d\gamma \dot{z}}{dt} = 0, \quad (3)$$

where \vec{r}_{\perp} and z are the transverse and longitudinal coordinates, respectively, of the instantaneous position $\vec{r} = (\vec{r}_{\perp}, z)$, $\gamma = (1 - \dot{r}^2/c^2)^{-1/2}$ is the Lorentz factor, and U a continuum potential. The integrals of the motion are

the total particle energy

$$E = m\gamma c^2 + U \quad (4)$$

and the longitudinal momentum

$$p_{\parallel} = m \gamma \dot{z} . \quad (5)$$

As a consequence, also the quantity

$$E_{\perp} \equiv E - (p_{\parallel}^2 c^2 + m^2 c^4)^{1/2} , \quad (6)$$

often termed the transverse energy, is conserved. It is easy to prove that, to an excellent approximation, the transverse energy assumes the form

$$E_{\perp} = \frac{1}{2} m \gamma_0 (\dot{x}^2 + \dot{y}^2) + U(x, y) , \quad (7)$$

and the transverse motion is described by the equation

$$m \gamma_0 \ddot{\vec{r}}_{\perp} + \nabla_{\perp} U(\vec{r}_{\perp}) = 0 . \quad (8)$$

Here $\gamma_0 = (1 - v^2/c^2)^{-1/2}$ is the initial value of the Lorentz factor γ .

The crystal structure and potential contours for the $\langle 110 \rangle$ direction in Si are shown in Fig.2. In the positive case, it is convenient to consider two types of particle, those with transverse energy small enough for them to remain in the unit cell, and those with larger transverse energy so that they wander from cell to cell. The former is referred to as proper channeled and the latter as channeled. The proper channeled particles are under the influence of several strings at the same time, and there is a tendency for

their motion to be regular, whereas the channeled particles are often under the influence of a single string at a time, and their motion tends to be chaotic. Negative particles, on the other hand, with $E_{\perp} < U_{\max}$ are bound to move around one string.

III.2. Doughnut scattering

The present paper is chiefly concerned with GeV electrons/positrons moving in directions close to axial directions. In such cases a special scattering mechanism, the doughnut scattering plays an important role. Conservation of transverse energy in collisions with individual atomic strings results, after a number of such collisions, in a rotation of the transverse momentum \vec{p}_{\perp} around the axial direction. In angle space, a parallel beam is therefore turned into a ring-shaped (doughnut) distribution with a radius ψ equal to the incident angle, after a certain number of collisions.

The crystal thickness λ_{\perp} needed for this equalization in the transverse plane was discussed already by Lindhard¹⁵ for incident angles $\psi < \psi_1$, where ψ_1 is the critical angle for axial channeling, i.e.,

$$\psi_1 = (4Z_1 Z_2 e^2 / d m c^2 \beta^2 \gamma)^{1/2}. \quad (9)$$

The parameter λ_{\perp} can be found from the equation

$$\frac{1}{\lambda_{\perp}} = 2N d \sin\psi \int_{-\infty}^{\infty} dl \sin^2\left(\frac{\varphi(l)}{2}\right) \quad (10)$$

where N is the atomic density, and $\varphi(l)$ is the scattering angle for an impact parameter l . For a $1/r$ -string potential, Lindhard gave the estimate

$$\lambda_{\perp} = \frac{4\psi}{\pi^2 N d a \psi_1^2} \quad \psi < \psi_1, \quad (11)$$

where a is the Thomas-Fermi screening distance. So for $\psi < \psi_1$, λ_{\perp} is propor-

tional to $\gamma\psi Z_2^{-1}$.

For incident angles $\psi > \psi_1$, a rather crude estimate for λ_{\perp} was found in ref.10a, i.e.

$$\lambda_{\perp} \approx \frac{4\psi}{\pi^2 N d a \psi_1^2} \left(\frac{4\psi^2 \rho}{\psi_1^2 a} \right), \quad \psi > \psi_1, \quad (12)$$

where ρ is the thermal vibrational amplitude which comes in because impact parameters smaller than ρ are excluded. From (12) it is seen that in this angular region, λ_{\perp} is proportional to $\gamma^2 \psi^3 Z_2^{-2}$, so the dependence on incident angle ψ and energy increases drastically when ψ gets larger than ψ_1 . The same dependence is obtained from eq.(10) for particles with transverse energy ($E_{\perp} = 1/2 m\gamma c^2 \beta^2 \psi^2$) well above the potential barrier, because here $\psi(1)$ is small and inversely proportional to E_{\perp} .

By numerical integration in eq. (10), λ_{\perp} can be found for other potentials^{10b}. The results of such calculations for two different potentials ($U(r) \propto 1/r, \ln(1+c^2 a^2/(r^2+\rho^2))$) are shown in fig.3a for 11.9 GeV protons incident on a $\langle 110 \rangle$ Ge crystal. The λ_{\perp} values are given as function of the incident angle ψ in units of ψ_1 . Clearly, λ_{\perp} increases very fast with ψ and is rather sensitive to the potential model. In ref.10, the estimates of (11) and (12) were compared to experimental results and binary-collision calculations. For $\psi < \psi_1$, the agreement is good but only fair for $\psi > \psi_1$. As is well known, the $1/r$ potential gives for fixed impact parameter the same scattering angle for positive and negative particles and thereby the same λ_{\perp} value. The large difference in doughnut scattering for positive and negative particles with incident angle $\psi > \psi_1$ can be seen in fig.3b. Here the exit distributions in azimuthal angles are approximated by Gaussians, from which an experimental width can be obtained. This approximation is found good for $\psi > \psi_1$. Evidently, the doughnut scattering is much more effective for negative par-

ticles as compared to positive. For $\psi < \psi_1$, λ_{\perp} values for negative particles are somewhat higher than those for positive particles.

In fig.4 are shown experimental results for 10 GeV/c protons transmitted through a 600 μm $\langle 110 \rangle$ Ge crystal. The plots show the exit-angle distributions for three different incident angle regions, namely: a(2-2.5) ψ_1 , b(3-3.5) ψ_1 , and c(3.5-4) ψ_1 . Typical λ_{\perp} values for $\psi < \psi_1$ are 5-10 μm (fig.3), whereas a 600 μm crystal barely gives complete equalization for incident angles (2-2.5) ψ_1 (fig.4a). The correlated scattering from the crystal axes is still very strong for incident angles of 4 ψ_1 , and the effect has been observed out to (10-15) ψ_1 . This has the very important implication that the continuum model can be used in the GeV region for incident angles much larger than ψ_1 .

In fig.5 are shown the results of computer simulations of the doughnut formation for 15-GeV/c protons and π^- penetrating a Ge crystal along the $\langle 110 \rangle$ direction. The equalization and the radial spread are here demonstrated for an incident angle of ψ_1 . The crystal thicknesses in μm are given above the scatter plots. For $\psi = \psi_1$, the radial scattering for negative particles results preferentially in a scattering towards smaller ψ values and filling up the dip around the axis, and eventually giving rise to a distribution with maximum along the axis. For protons, the doughnut is well conserved to very large thicknesses.

To complete the discussion of doughnut scattering, let us stress once more that this phenomenon is specific to continuum strings. As a consequence, when doughnuts are observed at incidence angles far beyond ψ_1 , this implies that the continuum description in such cases is valid in a wider region than that specific to channeling. To give an estimate, consider a particle incident on an atomic string at an angle ψ larger than ψ_1 , i.e., the trajectory is essentially a straight line. The basis for the continuum de-

scription is correlation in successive collisions with string atoms. Consequently, a necessary condition for correlation in at least two encounters with atoms of the same string is that the change in the impact parameter is less than approximately a or ρ in the passage from the first to the second atom. Applications of the continuum description at angle ψ beyond ψ_1 therefore requires $\psi < \rho/d$, which condition by means of eq. (9) reads

$$\beta^2 \gamma > 4Z_1 Z_2 \alpha^2 \frac{a_0 d}{e^2} \frac{m}{M_0} \left(\frac{\psi}{\psi_1}\right)^2 - \frac{m}{M_0} \left(\frac{\psi}{\psi_1}\right)^2$$

Here β and γ are the usual kinematical factors, and M_0/m denotes the ratio of the projectile-to-electron rest mass. For $Z_1^2=1$ and typical values of Z_2 , d and ρ (Si or Ge), the order of magnitude is given to the far right in (13). At relativistic energies, $\gamma > 1$, the inequality is always fulfilled beyond ψ_1 .

Obviously, a further condition for the actual observation of doughnuts is that the doughnut scattering is faster than random multiple scattering. Clearly, such channeling effects become increasingly important in the high-energy region because multiple scattering and dechanneling decrease as $(pv)^{-1}$, whereas channeling angles decrease only as $(pv)^{-1/2}$. Kudrin and Vorobiev^{10c} calculated the maximum incident angle ψ_m , for which doughnut scattering equals normal multiple scattering. For GeV particles, it turns out that $\psi_m \sim a/d$, incidentally in agreement with the simple criteria above.

III.3. Radiation from channeled particles

If the energy of the photons emitted by the projectile during the passage of the crystal is small compared to the primary energy, classical electrodynamics may be applied in the calculation of photon spectra. The spectral-angular distribution around a unit vector \hat{n} of the radiation from a

channeled particle can be calculated from¹⁶

$$\frac{d^2 I}{d\omega d\Omega} = \frac{e^2}{4\pi^2 c} \left| \int_{-\infty}^{\infty} \frac{\vec{n} \times [(\vec{n} - \vec{\beta}) \times \dot{\vec{\beta}}]}{(1 - \vec{\beta} \cdot \vec{n})^2} e^{i\omega(t - \vec{n} \cdot \vec{r}(t)/c)} dt \right|^2, \quad (14)$$

where $\vec{\beta}(t) = \dot{\vec{r}}(t)/c$ and $\vec{r}(t)$ is the position of the particle in the crystal. In the case of channeled particles, Avakian et al.¹⁴ were able to obtain a closed-form expression for Eq.(14) by approximating the potential by $U(r_{\perp}) = \alpha/r_{\perp}$ for $r_{\perp} > \rho$ and a constant for $r_{\perp} < \rho$. By using the dipole approximation, they were able to integrate Eq.(14) over the transverse energy distribution to obtain a spectral-angular density which can be compared with experiment. Because of the chaotic nature of the channeling motion, a rather broad spectrum is to be expected, and their result confirms this expectation.

For proper channeling, the equations of motion are given by (8). The particle trajectories can be described in the four-dimensional phase space, but since transverse energy is conserved in the continuum model, the individual trajectories are confined to three-dimensional manifolds of constant energy. There are two simple periodic solutions of Eq. (8), given by

$$m\gamma_0 \ddot{y} + \frac{\partial U}{\partial y}(0, y) = 0, \quad x = 0 \quad (15a)$$

and

$$m\gamma_0 \ddot{x} + \frac{\partial U}{\partial x}(x, 0) = 0, \quad y = 0. \quad (15b)$$

Since the motion is periodic, the radiation from these trajectories can be treated as in the planar case discussed in I. In particular, for fixed E_{\perp} , the maximum photon energy ω_m is in the forward direction, and

$$\omega_m(E_{\perp}) = \frac{4\pi n \gamma_0^2}{P(E_{\perp}) \left(1 + \frac{2\gamma_0^2 \bar{K}_{\perp}(E_{\perp})}{mc^2}\right)} \quad (16)$$

where P and \bar{K}_{\perp} are the period and average transverse kinetic energy corresponding to Eqs. (15).

If these periodic solutions are stable and if the spread in ω_m is not too large, then an experiment with good angular resolution should see their effects. Calculations¹⁷ show that for $x=0$, the periodic solution is stable in the proper channeling region, i.e., for $E_{\perp} < E_{\perp 1} = 4.6$ eV, the low saddle-point energy of the $\langle 110 \rangle$ channel (see fig.2). Periodic motion is also more or less stable in the y direction for $E_{\perp} < E_{\perp 2} = 22.6$ eV - the second-saddle point energy. For $y=0$, periodic solutions have a regime of stability for $E_{\perp} < E_{\perp 1}$ but are unstable for $E_{\perp} > E_{\perp 1}$. These various features could also be expected from a study of fig.2. In fig.6 is shown ω_m (eq.(16)) as a function of the transverse amplitude for stable motions of 5-GeV/c positrons oscillating in the y direction. From this, a photon peak around 17 MeV is expected for a suitable cut in the incident-angle space.

The total emitted power is given by the Lienard formula¹⁶

$$I = - \frac{d\varepsilon}{dt} = \frac{2}{3} \frac{e^2}{c} \gamma^6 [\dot{\beta}^2 - (\vec{\beta} \times \dot{\vec{\beta}})^2]. \quad (17)$$

Here it should be mentioned that although eq. (17) does not include coherent addition, it gives the correct value of the total radiated power and can be used as a check. In the continuum model, eq. (17) may be rewritten as

$$I = \frac{2}{3} \frac{e^2}{m^2 c^3} \gamma_0^2 |\nabla_{\perp} U(\vec{r}_{\perp})|^2. \quad (18)$$

For a beam of axially channeled electrons/positrons, the intensity averaged

over time can be found by integrating (18) over the transverse plane weighted for difference in particle entry points.

In a sufficiently thick target, the projectiles will reach the equilibrium distribution, where it is equally likely to find the particle in any of the accessible points of the transverse plane where $U(r_{\perp}) \leq E_{\perp}$. The average intensity is then obtained as the average over this area

$$\langle \frac{dI}{dl} \rangle (E_{\perp}) = A(E_{\perp})^{-1} \int_{A(E_{\perp})} d^2 \vec{r}_{\perp} \frac{2e^2}{3m^2 c^4} \gamma_0^2 |\nabla_{\perp} U(\vec{r}_{\perp})|^2, \quad (19)$$

where $A(E_{\perp})$ denotes the accessible area in the transverse plane. For electrons, the integration contains the axis, whereas a small area around the string is excluded for positrons. When the projectiles enter a crystal at an angle ψ to the string, the transverse energy inside the target attains the value

$$E_{\perp} = E_{\perp}(\vec{r}_{\perp 0}, \psi) = \frac{1}{2} \gamma_0 m c^2 \psi^2 + U(\vec{r}_{\perp 0}), \quad (20)$$

where $\vec{r}_{\perp 0}$ denotes the entrance point. To obtain the observable intensity, we therefore take the average of eq. (19) over $\vec{r}_{\perp 0}$,

$$\langle \frac{dI}{dl} \rangle (\psi) = A_0^{-1} \int_{A_0} d^2 \vec{r}_{\perp 0} \langle \frac{dI}{dl} \rangle (E_{\perp}(\vec{r}_{\perp 0}, \psi)), \quad (21)$$

where $A_0 = (Nd)^{-1}$ is the area occupied by each string.

When the transverse energy exceeds the potential height, the projectile may enter any point of the transverse plane, which means that the intensity becomes independent of the angle. Then the intensity is given by (19) with $A(E_{\perp}) = A_0$ and electrons give the same result as positrons.

The intensity of radiation emitted by positrons and electrons incident at an angle ψ to the $\langle 110 \rangle$ axis in Si is shown in fig.7, using the random-string model. In this model, the continuum potential is rotationally symmetric and cut off at a distance r_0 , given by $A_0 = \pi r_0^2$. The curves clearly show the difference in behaviour of channeled positive and negative particles, i.e., positrons are steered away from the atomic strings, whereas electrons are focussed around the strings. It should be noticed that the FWHM for electrons is less than half the FWHM for positrons as in wide-angle scattering experiments for MeV electrons/positrons.

The energy radiated per unit frequency and solid angle was given by eq. (14) or the equivalent¹⁶

$$\frac{d^2 I}{d\omega d\Omega} = \frac{e^2}{4\pi^2 c} \left| \int_{-\infty}^{\infty} \frac{d}{dt} \left[\frac{\vec{n} \times (\vec{n} \times \vec{\beta}(t))}{1 - \vec{n} \cdot \vec{\beta}(t)} \right] e^{i\omega(t - \vec{n} \cdot \vec{r}(t)/c)} dt \right|^2. \quad (22)$$

This shows that the total emitted radiation is obtained as the square of a time integral along the particle path, i.e., the radiation from different parts of the trajectory has to be added coherently. In the planar case described in I, this was simple because of the periodic motion of planar-channeled particles. In the present axial case, the integration is much more complicated. Fortunately, it turns out that often it suffices to integrate only along segments of the path and then add incoherently these contributions. For decreasing photon energy, the required length of the individual segments increases, and for very small frequencies, it is necessary even to add coherently the contribution from neighbouring strings¹⁸. For high photon energies, however, it turns out that the radiation from the collision with one single string can be found by adding incoherently the contribution from small parts of the track around the string. The radiation is emitted within an angle of $\sim 1/\gamma$, and the scattering angle in a single string collision is

of the order of ψ_1 . If $\psi_1 > 1/\gamma$, a distant detector will only receive an appreciable signal from a path length over which the acceleration is nearly constant. Furthermore, the acceleration may be considered orthogonal to the direction of motion. The spectrum observed in a given direction will be essentially the same as the synchrotron radiation from a circular motion with radius given by the local curvature of the trajectory^{2b}. For cases where the quantum recoil is negligible the synchrotron approximation represents a simple method for calculating radiation spectra based on the well known classical formula for synchrotron radiation weighted by the particle distribution. Taking into account the recoil complicates the situation and the more general description by Baier et al.⁹ should be considered. Kimball and Cue in a qualitative way introduced the recoil effect into the synchrotron approximation^{2b}.

IV. Discussion of results and comparison with theory

Radiation produced by electrons and positrons incident on a crystal with a direction close to a crystalline axis displays a very complicated dependence on the incident angle. Colour pictures in fig.8a,b and c show the intensity of 10 to 40 MeV photons emitted by 4.8 GeV/c e^+/e^- passing through Si and Ge crystals close to the $\langle 110 \rangle$ axis as function of the incident angle (θ_x, θ_y) . The white circles have a radius of ψ_1 (210 μrad for Si and 310 μrad for Ge) and are centered on the axes. Intensity goes from black/blue (low) over green and yellow to red (high). The scales are linear, but the levels on the three pictures cannot be compared as the colour scales have been chosen to give maximum contrast. The pixel size on the pictures is $20 \times 20 \mu\text{rad}^2$, corresponding to the angular resolution of the setup. For comparison is shown in fig.8d the intensity distribution in incident angle space for 10

GeV/c protons transmitted through a 0.57 mm thick $\langle 110 \rangle$ Ge crystal acting as an intrinsic detector. The energy-loss spectrum for the whole beam (± 1 mrad) is shown in the upper corner together with the slice (red region) used, i.e., channeled particles. The contrast in colours from pixel to pixel shows that the angular resolution from the drift chambers is better than the pixel size ($20 \times 20 \mu\text{rad}^2$).

Figure 8c shows the intensity of radiation emitted by 4.8 GeV/c electrons passing through a 100 μm Si crystal. A strong enhancement is seen for well aligned electrons as the only feature of the picture. This is as expected, as the electrons are trapped in a deep, steep potential well and focused around the axis. The intensity distribution is expected to be dependent on the energy window for the emitted photons, which is discussed below.

The distribution in radiation intensity (10-40 MeV photons) produced by 4.8 GeV/c positrons is much more complicated as can be seen in figs. 8a and b, where fig. 8a corresponds to a 100 μm thick $\langle 110 \rangle$ Si crystal and fig. 8b to 205 μm thick $\langle 110 \rangle$ Ge crystal. Well channeled (axial and planar) particles emit a relatively small amount of radiation in the present energy window. This is expected because most such particles have little transverse energy and move only in the flat portions of the axial or planar potentials. So the acceleration is small, and thereby little radiation is emitted. As the incident angle increases, the positrons begin to move into the steep part of the potential, and the radiation intensity increases. For the axial case, the dramatic enhancement from around $1/2\psi_1$ to $\sim 2\psi_1$ is caused by the strong doughnut scattering. The strong enhancement regions (red) are "cut" through by the planes, but it is also clear that the planar effects gradually disappear close to the axial region. This is a well known channeling effect found in other channeling experiments like low-energy loss transmission (fig. 8d). This transition region (axial-planar) was already discussed in the classical

channeling paper by Lindhard¹⁵ as the "string of strings" region. It will be discussed further below.

The crystalline planes seem more pronounced in fig.8a than in fig.8b, which is mainly caused by the fact that the axially channeled particles cover a smaller part of the incident beam in angular space, as the critical angle for Ge is 50% larger than the critical angle for Si. On the other hand, the details within the critical angle ψ_1 are best seen in fig.8b. A strong dependence on the azimuthal angle is clearly seen. Dips are seen for directions corresponding to the {111}-planes and also, to some extent, for the {110} planes. The largest radiation intensity is found in the direction of the {100} planes.

The following sections give a detailed description of the experimental data and discuss the results in the light of the theoretical description summarized in sect. III. The present experimental setup restricted the investigation to photons with an energy less than ~10% of the particle energy, so that classical calculations neglecting the photon recoil can be applied.

IV.1 Angular scans

Figure 9 shows the angular dependence of the emission of photons in the energy range 10-40 MeV for 4.8 GeV electrons and positrons passing through a 100 μm Si crystal near the $\langle 110 \rangle$ axis. The energy window is the same as that used for the colour pictures, fig.8. Part (a) displays the emission probability, part (b) the radiated power. The two representations look similar, as the variation of the enhancement over random is rather smooth in the interval 10-40 MeV. Well channeled positrons move through the crystal undergoing soft collisions with the strings and emitting a small amount of radiation. The amount of low-energy photons reaches a maximum for incident angles of the order of the critical angle ψ_1 . For electrons, the maximum is

obtained at small incident angles, where they move deep down in the steep axial potential. Calculations of the average radiated energy, as shown in fig.7, are qualitatively in agreement with the experimental data for small incident angles. The constant level predicted for large angles is not seen in fig. 9, which shows a decrease outside ψ_1 . This is not a contradiction but reflects the fact that the experimental data are restricted to the low-energy end. The total energy radiated on average (eq.(17)) is predicted to reach the constant level of 25 MeV in the present case, whereas it is less than 1 MeV for the results in fig.9. We note that at large angles, $\psi > 3\psi_1$, the electron and positron data nearly merge.

From eq.(22), a simple estimate can be obtained for how the low-energy part of the photon spectrum varies when the incident angle to the axis is increased. For a given frequency, the radiated energy is negligible if the phase factor goes through one or more cycles over the time where the front factor is large. This time δt may be estimated from the expansion

$$\left| \frac{\vec{n} \times \vec{\beta}}{1 - \vec{n} \cdot \vec{\beta}} \right| \approx \frac{2\gamma_0^2 \theta(t)}{1 + \gamma_0^2 \theta^2(t)} ; \quad \vec{n} \cdot \frac{\vec{\beta}}{\beta} = \cos\theta(t). \quad (23)$$

In the dipole limit $\gamma_0 \delta\psi \ll 1$, where $\delta\psi$ is the scattering angle in the collision with the string, the variation of the denominator in (23) may be neglected to lowest order because most of the radiation is emitted within an angle γ_0^{-1} from the average direction of motion. The front factor of eq.(22) is therefore significant when the acceleration is large. This corresponds to a time interval $\delta t \approx a/\psi c \approx a_0/\psi c$. Here ψ is the particle angle to the axis. The change in phase during this time δt is of the order of $\omega \delta t (1 - \beta) \approx \omega a_0 (2\gamma_0^2 \psi c)^{-1}$. The spectrum is nearly constant for frequencies where this estimate is small and falls off when the phase changes by more than one. Therefore, in the dipole limit, the extension of the spectrum can be charac-

terized by the frequency

$$\omega_1 = \frac{2\gamma_0^2 \psi c}{a_0} . \quad (24)$$

This simple estimate agrees with more accurate results obtained from a Coulomb-like string potential¹⁴. For angles well above ψ_1 , the intensity of soft photons should fall off as ψ^{-1} since the integral over frequencies is independent of the angle, cf. fig.7. This feature is evident from fig.9, for which case ω_1 assumes a value beyond the endpoint of the integration for $\psi > \psi_1$.

Angular scans similar to fig.9 are shown in fig.10 for 10 GeV/c electrons and positrons (emission probability) and 20 GeV/c positrons (power), here including photons with an energy less than 1.45 GeV. The data are taken from an earlier experiment WA64. A description of the experimental setup can be found in ref.19. Data for planar channeling from this experiment have previously been published in I. The angular resolution in WA64 was not as good as in the setup described above, being 58 μ rad at 10 GeV and 38 μ rad at 20 GeV, compared to critical angles for channeling along the $\langle 110 \rangle$ axis in Si of 150 μ rad at 10 GeV and 100 μ rad at 20 GeV. The resolution has smeared the angular scans somewhat. The difference in yields for 10 GeV/c electrons and positrons at large incident angles could be influenced by experimental problems.

IV.2. Classical versus Born approximation

As discussed in connection with doughnut scattering, the continuum model applies in a wide angular region beyond the channeling angle at GeV energies. Consequently, a description in terms of classical electrodynamics is valid for the motion of a charged GeV projectile impinging on an aligned

single crystal at an angle considerably larger than ψ_1 and, as long as the quantum recoil may be neglected, for its emission of radiation. This feature is revealed by a comparison of the experimental data of fig. 10b with the theoretical curve superimposed on the plot. As long as the photon energy is smaller than $\hbar\omega_1$, the change in phase during a string collision may be neglected. This corresponds to taking the zero-frequency limit in eq. (22), whereby the intensity depends only on the change in $\vec{\beta}$ caused by the collision. In the present case, $\hbar\omega_1$ attains the value 1.2 GeV ψ/ψ_1 , which is beyond the endpoint energy of 1.45 GeV as soon as ψ is somewhat larger than ψ_1 . Consequently, in obtaining the curve in fig. 10b, we have applied eq. (22) for $\omega=0$ and, in turn, averaged over all string collisions in a random-string model. Recoil corrections are smaller than 10% and have been neglected. Clearly, the simple classical curve reproduces nicely the experimental data for $\psi > \psi_1$ and all the way out to the maximum angle of $\sim 20\psi_1$.

The amount of bremsstrahlung emitted by an electron or a positron penetrating an amorphous substance or a single crystal in directions not too close to low-index crystallographic axes or planes may also be evaluated in the quantum-mechanical perturbation limit, cf. refs. 20 and 1. For channeled particles, on the other hand, the Born approximation is invalid because of the strong scattering on continuum strings which appears as a result of correlations in consecutive atomic encounters; the motion is governed by the continuum lattice. A minimum requirement for application of the perturbation treatment therefore is $\psi > \psi_1$. Outside the channeling region, the motion is essentially free, the small deflections $\Delta\psi \ll \psi$ encountered when the projectile passes close to a continuum string being of order

$$\Delta\psi = \frac{1}{\gamma} \frac{U_0}{mc^2} \frac{1}{\psi}, \quad (25)$$

where U_0 denotes the depth (or height) of the potential at the string. In

order to use the Born approximation, it is necessary that the full path is contained inside the radiation cone (independence of sign of projectile charge). This requires $\Delta\psi < 1/\gamma$, which is equivalent to the condition

$$\psi > \theta_0 \equiv \frac{U_0}{mc^2} \quad (26)$$

In total, application of the Born approximation demands incidence angles in excess of the larger of ψ_1 and θ_0 .

The characteristic angle θ_0 is independent of incidence energy, whereas the critical channeling angle scales as $\gamma^{-1/2}$. Hence, at high energies, the condition (26) is the most restrictive. The impact energy, at which ψ_1 becomes equal to θ_0 , corresponds to a γ value of roughly

$$\gamma_{th} \equiv \frac{2mc^2}{U_0} \quad (27)$$

since, approximately, we have $\psi_1 = \sqrt{(2U_0/mc^2)\gamma\beta^2}$. For the $\langle 110 \rangle$ axis in silicon and germanium, the threshold energy $E_{th} \equiv \gamma_{th} mc^2$ equals 3.4 GeV and 1.8 GeV, respectively, at a temperature of 100K. At the impact energies of the accompanying experiments, θ_0 therefore exceeds ψ_1 . It assumes values of 0.3 mrad for the $\langle 110 \rangle$ axis in silicon at 100K and 0.6 mrad for the same axis and temperature in germanium.

In fig. 10b, we have plotted the results of a Born calculation for three different polar angles to the silicon $\langle 110 \rangle$ axis. To simulate the averaging over the azimuthal angle, which has been performed for the experimental data, coherent bremsstrahlung spectra have been computed for two different but random azimuthal angles of 0.15 and 0.25 relative to the $\{110\}$ plane, and the displayed results constitute the mean value (variations are less than 10%). Clearly, the bremsstrahlung intensity obtained in the Born approxima-

tion agrees nicely with the experimental data at large angles. Also, we see that the perturbation treatment tends to overestimate the yield when the characteristic angle θ_0 is approached, cf. the point plotted at the lowest angle.

In its final form, fig. 10b displays a unique situation: At incidence angles beyond θ_0 (dipole limit), a lowest-order Born approximation and a purely classical calculation yields the same radiation! Both are in good agreement with experiments.

IV.3. Radiation spectra - doughnut scattering and coherence

The general structure of the radiation spectra for 4.8 GeV/c electrons and positrons incident along the $\langle 110 \rangle$ axis in Si and Ge is shown in fig. 11. The spectra cover the region $(0-1.5)\psi_1$ in steps of $\psi_1/3$ and $\psi_1/4$. Top and middle row is for electrons/positrons incident on a 100 μm Si crystal, and the bottom row is for positrons incident on a 205 μm Ge crystal. In general, the spectra show a strong enhancement, up to a factor 50, with respect to incoherent bremsstrahlung over a broad range of photon energies. Electrons emit the largest amount of radiation when they are well channeled, whereas the maximum for positrons appears for incident angles close to ψ_1 , as discussed above in connection with fig. 8. Dechanneling and multiphoton production is much stronger for the Ge crystal than for the Si crystal, which in part is responsible for lower enhancement in Ge. Multi-photon production results in an increase of the total intensity at large photon energies, which, at least partly, explains that the photon-spectra for Ge show an increase for incident angles close to ψ_1 , where the Si spectra show a constant level. It is clearly seen that well channeled positrons predominantly produces low-energy photons (in this case, $E_\gamma = 15$ MeV), and the range of photon energies as well as the intensity increases as the incident angle to the axis in-

creases. A general feature of all the spectra is the pronounced dip in yield for small photon energies. This dip in the photon spectra was discussed in detail in ref.18, where it was shown to be due to doughnut scattering. Coherence is maintained over a length l_{coh} where the variation in the phase factor is less than unity. Using $1 - \beta_{\perp}^2 (2\gamma_0^2)^{-1}$ and that the radiation is emitted within an angular cone of $\sim 1/\gamma_0$ we have in the dipole limit ($\gamma_0 \delta\psi \ll 1$)

$$l_{\text{coh}} = l_{\omega} = \frac{\gamma_0^2 c}{\omega} \quad (28)$$

When the radiation is calculated, its path in the crystal is naturally split up into sections of length l_{ω} , and the contributions from different sections add incoherently. For small photon frequencies eq. (23) is dependent only on initial and final direction of the transverse velocity $\vec{\beta}_{\perp}$. A parallel beam of GeV particles incident on a crystal with an angle ψ to the axis develops after a crystal thickness λ_{\perp} into a doughnut with radius ψ . Here, where a uniform distribution in angle space has developed, the intensity of channeling radiation saturates. For crystals thicker than λ_{\perp} , a suppression in the photon intensity sets in due to coherent superposition, because for $l_{\omega} > \lambda_{\perp}$, only the fraction $\lambda_{\perp}/l_{\omega}$ of the crystal is effective in the radiation process. A more precise calculation of the reduction can be found in ref.18. A dip in photon yield is expected for $\omega \rightarrow 0$ and since $\lambda_{\perp}/l_{\omega} \propto \omega$, the intensity will increase linearly with ω until $\lambda_{\perp} \sim l_{\omega}$, which corresponds to a characteristic energy

$$h\omega_{\perp} = \frac{\hbar c \gamma_0^2}{\lambda_{\perp}} \quad (29)$$

For the case of 5 GeV/c electrons/positrons incident on $\langle 110 \rangle$ Si and Ge

crystals (fig.11), $\gamma\psi_1$ equals 1.96 and 2.95, respectively, so the condition for the dipole approximation is not fulfilled. Figs.11a,f,k belong to the transition region $\gamma\psi \approx 1$. This region was investigated by Pedersen et al.¹⁸, using Monte Carlo calculations for the cases $\gamma\psi_1=2$ and $\gamma\psi=2/3$ and $4/3$. The calculation shows a somewhat less pronounced suppression for small frequencies but some reduction remains even for $\omega > \omega_{\perp}$.

In fig.11, the channeled electrons show a much more pronounced reduction than the positrons. The main reason is that for axially channeled electrons, the velocity is periodic. For small frequencies, eq.(23) is only dependent on initial and final velocity $\vec{\beta}_{\perp}$. This means that one oscillation and many oscillations give the same coherent radiation, and a strong reduction at low photon energies is expected as for the planar case.

Axially channeled positrons do not have periodic motion, so the reduction for low photon energies in the positron cases is due to equalization in the doughnuts. From eq.(11), λ_{\perp} -values for $\psi=\psi_1$ can be estimated for Si and Ge, giving 3 and 2 μm . The Monte Carlo calculation (fig.5) gives somewhat larger λ_{\perp} values. The corresponding width of the dip λ_{\perp} is from eq.(29) around 6 MeV and 10 MeV for Si and Ge, respectively. For 1 MeV photons and 4.8 GeV electrons, l_{ω} is around 20 μm , compared to λ_{\perp} values of 2-3 μm , so that a pronounced dip should be found. The widths are expected to be somewhat broader than 6 MeV (Si) and 10 MeV (Ge) because in the present cases $\gamma\psi \approx 1$. The reduction $\lambda_{\perp}/l_{\omega}$ is indeed proportional to ω , as seen in figs. 11h,i,j,m,n, and o but not in the low transverse-energy positron data (f,g,k,l). This can be understood by remembering that positrons with small E_{\perp} values can have periodic motion inside a channel, and pure doughnut effects are obtained only for $\psi > \psi_1/2$, which can also be seen from the colored pictures in fig.8. The special motion for proper channeled positrons is discussed below.

There is a clear difference in the electron dips as compared to the positron ones for increasing incident angle ψ . Already for $\psi > \psi_1/2$, the electron dips start to disappear, whereas those for positrons stay beyond ψ_1 . This is in agreement with the results shown in fig.5., where negative channeled particles have a very pronounced radial scattering which will smear the coherence, and clearly λ_1 for positrons in this angular region is smaller than for electrons, giving a more pronounced reduction.

IV.4. Multiple scattering and coherence

For electrons/positrons traversing thin crystals with high energies, $\gamma\psi_1 > 1$, another reduction mechanism for low photon energies comes into play - the so-called Landau-Pomeranchuk effect²¹. This was also discussed by Pedersen et al. in ref.8. The effect corresponds to a suppression of the coherent radiation due to multiple scattering. In ref.16, it is shown that the radiation intensity $dI/d\omega$ emitted in a collision, where the velocity changes by $\Delta\vec{\beta}$, is proportional to $\gamma^2 |\Delta\vec{\beta}|^2$. This relationship, however, only holds for $|\Delta\vec{\beta}|^2 < 2/\gamma$. Above this limit, the coherence is destroyed, and the angular distribution of the radiation will be like two search-light beams, one centered around the initial direction and the other around the final direction of the projectile. In that case, the emitted intensity $dI/d\omega$ is proportional to $\ln\gamma$ for small frequencies.

For doughnut scattering, the maximum scattering angle is 2ψ , and the criterion $|\Delta\vec{\beta}|^2 < 2/\gamma$ will always be fulfilled in the dipole limit, implying that $dI/d\omega \propto |\Delta\vec{\beta}|^2$. For $\psi\gamma > 1$, the criterion $|\Delta\vec{\beta}|^2 < 2/\gamma$ gives a characteristic length $l_{1/\gamma}$, which is the penetration depth corresponding to a total scattering angle of $2/\gamma$. In the following, incident angles ψ less than $\sim 5\psi_1$ are considered. This means that doughnut scattering is the relevant scattering process. In such cases, the three-dimensional scattering angle amounts to

$\theta = 2\psi \sin\phi/2 \approx \psi\phi$, where ϕ is the azimuthal scattering angle in the transverse plane. The limit

$$\theta = \psi\phi = 2/\gamma \quad (30)$$

leads to a characteristic length of

$$l_{1/\gamma} \approx \left(\frac{\omega}{2\pi}\right)^2 \lambda_{\perp} = \frac{\lambda_{\perp}}{\gamma^2 \psi^2 \pi^2} \quad (31)$$

If $l_{1/\gamma}$ is shorter than l_{ω} , a reduction in intensity for small photon energies is expected. Laskin et al.^{21b} discussed this situation, and a simple expression for the coherence length l_{coh} is obtained (Pedersen et al.⁸) in terms of $l_{1/\gamma}$ and l_{ω} from the dipole limit i.e.,

$$l_{\text{coh}} = (l_{\omega} l_{1/\gamma})^{1/2} \quad (32)$$

giving the reduction factor R_{LP} due to the Landau-Pomeranchuk effect

$$R_{\text{LP}} = l_{1/\gamma}/l_{\text{coh}} = (l_{1/\gamma}/l_{\omega})^{1/2} \quad (33)$$

Here it should be noted that R_{LP} is proportional to $\omega^{1/2}$ whereas the reduction due to equalization in the doughnut is proportional to ω . Therefore it should be possible to distinguish the two types of suppression from the slope of the dips. The width of the last type of dip can also be estimated just by setting $R_{\text{LP}}=1$ in eq.(33), giving

$$k\omega_{\perp}^{\text{LP}} \propto \gamma^{5/2} \frac{\psi_1}{\psi} \propto \gamma^2 \psi^{-1} \quad , \quad \psi > \psi_1 \quad (34)$$

cf. eq. (12).

In fig.12 are shown photon spectra for 5-, 10- and 20-GeV/c positrons transmitted through a 100 μm $\langle 110 \rangle$ Si crystal with an incident-angle region of $0-\psi_1$ around the $\langle 110 \rangle$ axis. The $\gamma\psi_1$ values are given in the figures, showing cases above the dipole limit. For the 20-GeV/c positrons, $l_{1/\gamma}$ can be found from eq.(31), giving a value less than 1 μm for a 10-MeV photon energy, so the strong reduction for 10- and 20-GeV/c positrons is due to scattering from doughnuts. It is also clear that the dips broaden for increasing energy, which is in agreement with the $\omega^{1/2}$ dependence.

From eqs. (33) and (34) it is seen that the reduction R_{LP} is proportional to $(\omega/\omega_{LP}^1)^{1/2}$, and the width is proportional to $\gamma^2\psi^{-1}$. Experimentally this was investigated for 10 and 20 GeV/c electrons and positrons transmitted through a 100 μm thick Si crystal. The results are shown in fig.13 (10-GeV/c electrons), fig.14 (10-GeV/c positrons) and fig.15 (20-GeV/c positrons), where photon spectra are given for increasing incident angle ψ to the $\langle 110 \rangle$ axis with a step size of $1/2 \psi_1$. Like in fig.11, channeled electrons (figs. 13a and b) give pronounced dips for low photon energies (notice the energy scale) due to the bound motion. For $\psi > \psi_1$, 10-GeV/c electrons and positrons show the same moderate dip.

The γ dependence is clear by comparing figs.14 and 15. The dips for 20 GeV/c are the most pronounced with a width of around 200 MeV, whereas those for 10-GeV/c positrons are between 50 MeV and 100 MeV, in qualitative agreement with expectation.

The ψ dependence, however, is not so clear, but it should be borne in mind that all spectra in figs. 13, 14 and 15 are performed by circular integration around the $\langle 110 \rangle$ axis, so planar radiation is included. The strong enhancements from planar channeling radiation for 10-20 GeV/c electrons/positrons appear around 100 MeV photon energies and will tend to smear the dips.

For an incident angle ψ much larger than ψ_1 , the doughnut scattering disappears, and the Landau-Pomeranchuk effect for amorphous foils should be seen. In fig.16 are shown photon spectra for 20 GeV/c positrons incident on the 100 μ m thick $\langle 110 \rangle$ Si crystal. The spectra are again obtained by circular integration around the $\langle 110 \rangle$ axis but here in steps of $2\psi_1$ with a maximum radius of $12\psi_1$, where doughnut effects for Si are weak. Clearly, there is a pronounced dip which for the first figs. (a,b) increases in width with increasing angle ψ . From there on, the width is practically constant (200 MeV). Therefore the strong suppression of low-energy photons in figs. d, e, and f is partly due to a Landau-Pomeranchuk effect for amorphous targets.

IV.5. Radiation from proper channeled particles

From the colored pictures in fig.8 it is clear that there is a strong variation in the radiation spectra for incident angles ψ smaller than ψ_1 , especially when the azimuthal angle is varied. These phenomena have been studied by the production of spectra where the incident angles are restricted to certain azimuthal angular ranges. The investigations were performed by 4.8-GeV/c positrons transmitted through the 100 μ m thick $\langle 110 \rangle$ Si crystal. Here the channeling angle ψ_1 equals 208 μ rad, and the angular resolution was 20 μ rad, so detailed scans are justified. In fig.17 are shown spectra with restriction in azimuthal angle. The top row covers the range 0 to $1/3 \psi_1$ to the axis, and the bottom row covers the range $2/3 \psi_1$ to ψ_1 . In the right column are shown spectra where the azimuthal range has been restricted to a $\pm 15^\circ$ wedge around the $\{110\}$ direction, whereas the left column shows a $\pm 15^\circ$ angular region around the $\{100\}$ direction. These two directions were chosen because the surface of section calculations predicts stable periodic trajectories along these planes. Furthermore, fig.6 showed a peak around 17 MeV from the first harmonic for motion along the $\{100\}$ direction. A noticeable

difference is seen in the two spectra in the top row: Along the $\{100\}$ direction is in fact seen a peak around 17 MeV which is absent in fig.b. These spectra show for the first time that it is possible in the GeV region to steer positrons into special proper channeled motion, and channeling radiation might be one of the few situations, where such proper channeling can be identified.

The azimuthal variation is most pronounced, however, for incident angles close to ψ_1 , as seen in the bottom row of fig.17. The enhancement along the $\{100\}$ direction is very large, close to a factor 45, whereas it is around a factor 30 along the $\{110\}$ direction. In the $\{100\}$ direction, the positrons will be able to jump across the saddle point between the two closely spaced strings (see fig.2) and build-up coherent radiation. The path for these particles might start to look like the path for planar channeled positrons. In fact, the small bump in 17d) near 20 MeV could be the first sign of the first harmonic in planar channeling radiation along the plane.

IV.6. Radiation from the transition region: axial to planar channeling

The colored pictures in fig.8 or fig.11 in I show that the strong steering effect from crystal planes gradually disappears in an incident-angle region close to ψ_1 . This means that the pronounced peaks from first and second harmonics seen in planar channeling radiation (see I) should gradually turn into the structureless axial spectra. In fig.18 are shown photon spectra from 4.8 GeV/c positrons, where the incident angle to the $\langle 110 \rangle$ axis in the 100 μm thick Si crystal is between ψ_1 and $2\psi_1$. In the following columns, this angle is increased in steps of ψ_1 . In the upper row the incident angle to the $\{110\}$ plane is between 0 and $\psi_p/3$. The middle and bottom rows cover incident angles of: $2\psi_p/3-3\psi_p/3$ and $4\psi_p/3-5\psi_p/3$, respectively. The peak corresponding to the first harmonic in planar radiation develops

for incident angles around $2\psi_1$ to the $\langle 110 \rangle$ axis, which is in agreement with the classical channeling picture where axial motion has turned into planar motion for incident angles $\psi > 2\psi_1$. This is also in agreement with investigations of δ -ray yields from 11.9-GeV/c protons and μ^+ penetrating Si and Ge crystals close to the $\langle 110 \rangle$ axis²².

In general, the radiation level is high in the first column and decreases for increasing angle to the axis. For the planar channeled positrons (top and middle row), the intensity in the first harmonic is higher in the present spectra than what is obtained far from the axis (fig. 20 in I). The extra intensity in the present case is most likely due to incident particles that are dechanneled through the surface transmission. This amounts to around 15% of the incident positrons and they emit high intensity radiation due to doughnut scattering like those in the bottom row. This situation is different from a case far away from the axis, because then dechanneled particles do not give the enhancement in radiation around the first harmonic.

In the present situation, the radiation is a mixture of coherent bremsstrahlung and channeling radiation. In such cases, the combination of radiation should give rise to a spectrum where channeling peaks are surrounded by side bands²³. Observation of such side bands requires, however, a beam with a very well defined angle and could not be seen in the present experiment because of multiple scattering.

V. Conclusion

For axially channeled GeV electrons and positrons, the low-energy part of the photon spectra is enhanced by around a factor of 50 above the incoherent bremsstrahlung. The total emitted power is for electrons strongly

peaked around the axis, whereas positrons show a pronounced dip. The HWHM for the electron peak is only $1/3$ of ψ_1 , whereas the positron dip has a width of around ψ_1 , reflecting the difference in flux distribution inside the crystal for electrons and positrons. For low-energy photons (10-100MeV), the maximum emitted intensity is for electrons obtained for particles parallel to the axis, whereas positrons give maximum intensity for incident angles around ψ_1 , in fair agreement with calculations. The strong doughnut scattering give rise to a dramatic enhancement of the overall emitted radiation. In the dipole limit ($\gamma\theta\psi > 1$), the equalization in doughnut scattering gives rise to a pronounced reduction in low-energy photon yields for cases where the crystal thickness λ_1 needed for equalization in the doughnut is smaller than the coherence length l_w . Above the dipole limit, another type of reduction sets in from multiple scattering, which for scattering angle $\theta > 2/\gamma$ destroys the coherence. This effect becomes very pronounced for high energies (~ 20 GeV/c) and incident angles $\psi > \psi_1$. In random, this effect was predicted as the Landau-Pomeranchuk effect. For a crystal thickness $l_{1/\gamma}$ giving a multiple scattering $\theta = 1/\gamma$, the reduction is $(l_{1/\gamma}/l_w)^{1/2}$. Pronounced variations in radiation spectra are found for proper channeled positrons. For the first time, peaks are found in the axial radiation spectra, corresponding to stable motions parallel to the {100} planes. The energy of the peak is in fair agreement with theoretical estimates. In the transition region from axial to planar effects, the emitted radiation spectra change from the nearly structureless axial spectrum to a planar spectrum, with a pronounced first harmonic. This transition region ranges from around ψ_1 to $\sim 2.5\psi_1$, but the particles with $\psi > \psi_1$ enhance the general intensity level due to doughnut scattering.

Acknowledgements

The authors are grateful to J.U. Andersen and E. Bonderup for fruitful discussions and helpful criticism. We are especially indebted to members of the WA64 collaboration, who played an active part in the first channeling-radiation experiments at the SPS. P. Siffert is acknowledged for his enthusiasm in developing new detectors. The Danish participation was made possible by funds from The Danish Committee for Accelerator-Based Research.

References

- 1) G.Diambrini Palazzi, Rev.Mod.Phys.40 (1968) 611
- 2) a) V.Beloshitsky and F.F.Komarov, Phys.Rep.23 (1982) No.3.
 b) J.Kimball and N.Cue, Phys.Rep.125 (1985) No.2
 c) Coherent Radiation Sources, eds. A.W.Saens and H.Überall, Springer Verlag, Berlin, 1985
- 3) J.U. Andersen, E. Bonderup, and R.H. Pantell, Ann.Rev.Nucl.Part.Sci. 33 (1983) 453
- 4) J.Bak, J.A. Ellison, E. Marsh, F.E. Meyer, S.P. Møller, C.Pedersen, J.B.B. Petersen, M. Suffert, A.H. Sørensen, E. Uggerhøj, and K. Østergaard, Nucl.Phys.B 254 (1985) 491.
- 5) a) N.F. Shulga, L.E. Gendenstein, I.I. Miroshnichenko, E.V. Pegushin, S.P. Fomin and R.O. Avakian, Sov.Phys.JETP 55 (1982) 30
 b) M. Pisharody, Radiation from Multi-GeV Positron Channeling in Diamond, Thesis, Albany, USA
- 6) V.N. Baier, V. M. Katkov, and V.M. Strakhovenko Phys.Stat.Sol.(b) 133 (1986) 583
- 7) Proceedings of the 2nd-All-Union Conference on Electromagnetic Radiation of Relativistic Particles in Crystals. Rad.Effects 91 (1986) 163
- 8) Proceedings of the NATO Advanced Research Workshop on Relativistic Channeling, April 1986. Maratea, Italy. Eds. J.Ellison, and D. Carrigan, to be published
- 9) V.N. Baier, V.M. Katkov and V.M. Strakhovenko, Phys.Lett.A 114 (1986) 511. V.N. Baier, V.M. Katkov and V.F. Fadin, Radiation of Relativistic Electrons. Atomizdat, Moscow, 1973
- 10) a) S.K. Andersen, O. Fich, H.Nielsen, H.E. Schiøtt, E. Uggerhøj, C. Vraast Thomsen, G. Charpak, G. Petersen, F. Sauli, J.P. Ponpon, and P. Siffert, Nucl.Phys.B 167 (1980) 1

- b) H.Madsbøll, Thesis, Aarhus University, unpublished (1981)
- c) V.V. Kudrin and S.A. Vorobiev, Rad.Effects 25 (1975) 119
- 11) J.F. Bak, P.R. Jensen, H. Madsbøll, S.P. Møller, H.E. Schiøtt, E. Uggerhøj, J.J. Grob, and P. Siffert, Nucl.Phys.B 242 (1984) 1
- 12) A.O. Aganyants, Yu.A. Vartanov and G.A. Vartapetyan, JETP Lett. 42 (1985) 399
- 13) A. Belkacem, G. Bologna, M. Chevalier, N. Cue, M.J. Gaillard, R. Genre, J.C. Kimball, R. Kirsch, B. Marsh, J.P. Peigneux, J.C. Poizat, J. Reimilleux, D. Sillou, M. Spighel, and R.C. Sun, Phys.Lett.B 177 (1986) 211
- 14) A.L. Avakian, N.K. Zhevago, and Yan Shi, Sov.Phys.JETP 55 (1982) 341
- 15) J. Lindhard, K.Dan. Videnskab.Selskab Mat.Fys.Medd. 34 No.14 (1965)
- 16) J.D. Jackson, Classical Electrodynamics, John Wiley & Sons, New York 1975
- 17) a) C.E. Seal, Thesis, Albuquerque, NM, USA, unpublished
b) J.Su, Thesis, Albuquerque, NM, USA, unpublished
- 18) O. Pedersen, J.U. Andersen and E. Bonderup, Nucl.Instrum.Methods B 13 (1986) 27 and the same authors in ref.8.
- 19) M. Atkinson, J. Bak, P.J. Bussey, P. Christensen, J.A. Ellison, R.J. Ellison, K.R. Erikson, D. Giddings, R.E. Hughes-Jones, B.B. Marsh, D. Mercer, F.E. Meyer, S.P. Møller, D. Newton, P. Pavlopoulos, P.H. Sharp, R. Stensgård, M. Suffert, and E. Uggerhøj, Phys.Lett.B 110 (1982) 162
- 20) W. Heitler, The Quantum Theory of Radiation, Dover, New York, 1984
- 21) a) A.I. Akhiezer and N.F. Shulga, Sov.Phys.US PEKHI 25 (1982) 541
b) N.V. Laskin, A.S. Mezmanishvili and N.F. Shulga, Phys.Lett.A 112 (1985) 240
- 22) J. Bak, J.S. Forster, J.J. Grob, P.R. Jensen, H. Madsbøll, G. Melchart, S.P. Møller, G. Petersen, H. Schiøtt, P. Siffert, and E. Uggerhøj, Nucl. Phys.A 389 (1982) 533

23) a) V.V. Beloshitsky and M.A. Kumakhov, Rad.Eff.56 (1981) 25

b) H. Überall and A.W. Sáenz, Phys.Lett.A 90 (1982) 370

Figure Captions

Fig. 1. Setup for the PS188 experiment. SC designates scintillators, DC are drift chambers. BM are bending magnets, and NaI is the photon detector. The beam enters from the left.

Fig. 2. Contour plot of string potential for the $\langle 110 \rangle$ axis in silicon. Indicated energy levels are in eV and give the potential for positive particles. Changing the sign on the values gives the potential for negative particles. The two saddle points in the potential contours E_{1_1} and E_{1_2} are discussed in the text.

Fig. 3. (a) Calculated λ_1 -values for $\psi \gg \psi_1$ using different potentials:

$$(1) \quad U(r) = \frac{z_1 z_2 e^2}{d} \frac{\pi a}{2r}, \quad (2) \quad U(r) = \frac{z_1 z_2 e^2}{d} \ln\left(1 + \frac{C^2 a^2}{r^2 + a^2}\right)$$

when 11.9 GeV/c protons are incident on a $\langle 110 \rangle$ Ge crystal, which is 0.6 mm thick. (b) Width and distribution in exit azimuthal angles for 11.9-GeV/c protons and π^- transmitted through the 0.6 mm $\langle 110 \rangle$ Ge crystal.

Fig. 4. Three-dimensional scatter plots in exit-angle space of 10 GeV/c protons transmitted through a 0.6 mm thick $\langle 110 \rangle$ Ge crystal. The incident beam directions from the $\langle 110 \rangle$ axis are given in the figures. The center of the plots is the $\langle 110 \rangle$ direction and the scale is in mrad.

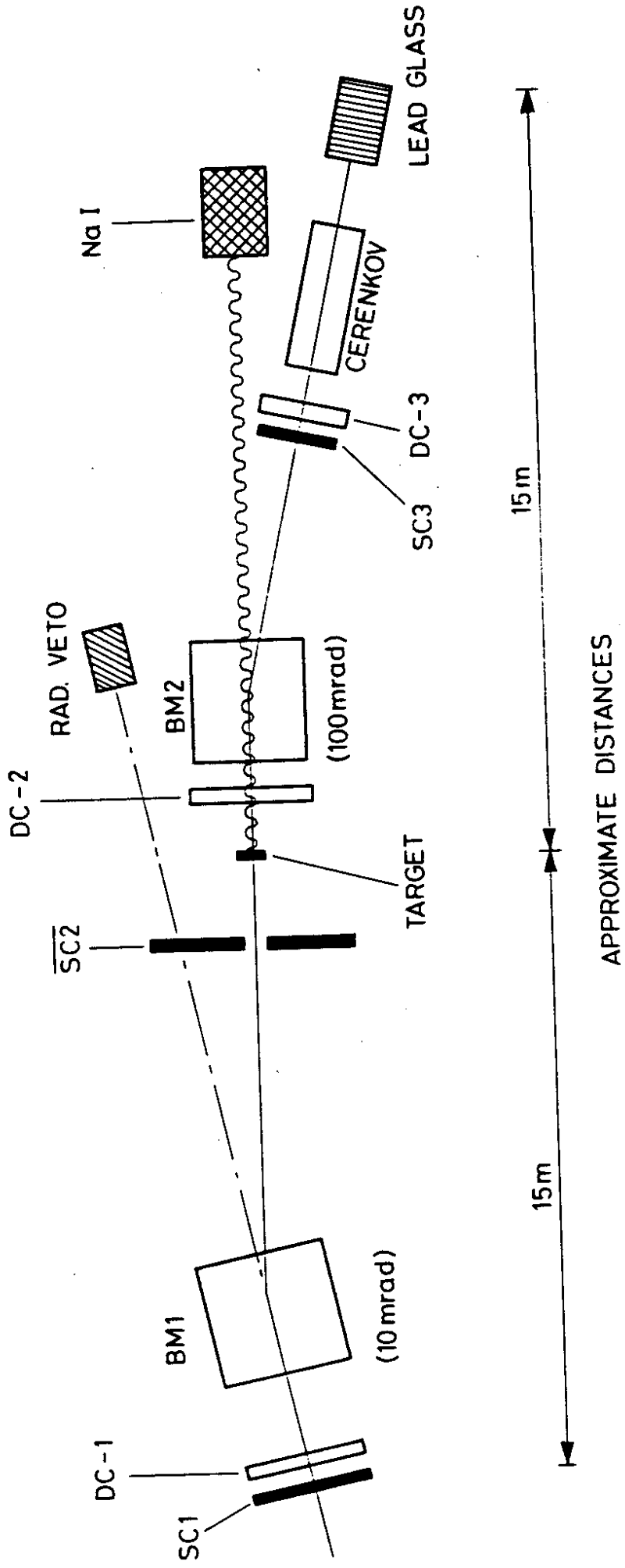
Fig. 5. Results of computer simulations for 15 GeV/c protons and π^- traversing increasing thicknesses of Ge. The incident angle to the axis is ψ_1 . Clearly protons attain equalization on a shorter distance than π^- . Similar calculations for incident angles of $2\psi_1$ and $3\psi_1$ can be found in ref.10a.

- Fig. 6. The maximum photon energy in the forward direction $M_{w_{\max}}$ for 5-GeV/c proper channeled positrons giving periodic solutions along the $\langle 100 \rangle$ direction. The photon energies are calculated for increasing amplitude (in Å), using a thermally average Doyle-Turner potential which takes into account the 24 neighbouring strings to the $\langle 110 \rangle$ channel.
- Fig. 7. Radiative energy loss for positrons (full drawn curve) and electrons (dashed curve) as a function of incident angle to the $\langle 110 \rangle$ axis in Si (in units of ψ_1). In the calculations, a random-string model is used.
- Fig. 8. Intensity distribution in two-dimensional incident angle space of 4.8 GeV/c positrons (a and b) and electrons (c) emitting (10-40) MeV photons when traversing a 100 μm thick $\langle 110 \rangle$ Si crystal (a and c) and a 205 μm thick $\langle 110 \rangle$ Ge crystal (b). Fig.d is a two-dimensional plot in incident angle space of those 10 GeV/c protons that have given a low-energy loss (indicated in red) in a 0.57 mm thick $\langle 110 \rangle$ fully depleted Ge detector. The circles indicate the size of the critical angle ψ_1 . The pixel (one of the small squares) correspond to $(20 \times 20) \mu\text{rad}^2$.
- Fig. 9. (a) Number of 4.8-GeV/c electrons/positrons emitting photons in the energy ranges (10-40) MeV as a function of incidence angle. (b) Same as (a), but here it is the emitted power in the range (10-40) MeV. The open circles correspond to 4.8 GeV/c electrons and solid circles to 4.8 GeV/c positrons.
- Fig. 10. (a) Probability distributions for 10-GeV/c electrons/positrons emitting (10-110)MeV photons in a 100 μm $\langle 110 \rangle$ Si crystal. (b) Angular distributions for 20 GeV/c positrons emitting photons in the energy region of 10 MeV-1.45 GeV. The full-drawn curve displays the

result of a classical estimate in the zero frequency limit. Triangles represent the result of a Born calculation.

- Fig. 11. Low-energy part of the photon spectra for 4.8 GeV/c electrons (a-e) and positrons (f-j, k-o) transmitted through a 100 μm thick $\langle 110 \rangle$ Si crystal (a-e, f-j) and a 205 μm thick $\langle 110 \rangle$ Ge-crystal (k-o). The incident angle regions around the $\langle 110 \rangle$ axis (circles) are given at the top of each column.
- Fig. 12. Low-energy part of the photon spectra for 4.8 GeV/c (a), 9.6 GeV/c (b) and 20 GeV/c (c) positrons transmitted through a 100 μm thick Si crystal in an incident angle region of $(0-\psi_1)$ around the $\langle 110 \rangle$ axis. The ψ_1 -values are given in the figures.
- Fig. 13. Radiation spectra for 10 GeV/c electrons incident on a 100 μm thick $\langle 110 \rangle$ Si crystal. The spectra a to f are obtained for increasing incident angle to the $\langle 110 \rangle$ axis, where fig.a covers angles $(0-0.5)\psi_1$, b: $(0.5-1.0)\psi_1$, c: $(1.0-1.5)\psi_1$, d: $(1.5-2.0)\psi_1$, e: $(2.0-2.5)\psi_1$, f: $(2.5-3.0)\psi_1$.
- Fig. 14. Same as fig.13 but for 10 GeV/c positrons.
- Fig. 15. Same as fig.13 but for 20 GeV/c positrons.
- Fig. 16. Same as fig.15 but here the incident angle steps are a): $(0-2)\psi_1$, b): $(2-4)\psi_1$, c: $(4-6)\psi_1$, d: $(6-8)\psi_1$, e: $(8-10)\psi_1$, f: $(10-12)\psi_1$.
- Fig. 17. Azimuthal variation in channeling radiation spectra produced by 4.8 GeV/c positrons incident on a 100 μm thick $\langle 110 \rangle$ Si crystal inside ψ_1 . a): $(0-1/3)\psi_1$, 15° around the $\{100\}$ direction, b): $(0-1/3)\psi_1$, 15° around the $\{110\}$ direction, c): $(2/3-3/3)\psi_1$, 15° around $\{100\}$ direction, d) $(2/3-3/3)\psi_1$, 15° around $\{110\}$ direction.
- Fig. 18. Photon spectra from 4.8 GeV/c positrons incident on the 100 μm thick $\langle 110 \rangle$ Si crystal for varying incident angle to the $\langle 110 \rangle$ axis and the $\{110\}$ plane. The top row corresponds to $(0-1/3)\psi_p$ to the

(110) plane, middle row: $(2/3-3/3)\psi_p$ and bottom row: $(4/3-5/3)\psi_p$.
On top of each column is given the incident angle region to the
<110> axis.



127-324

FIG. 1

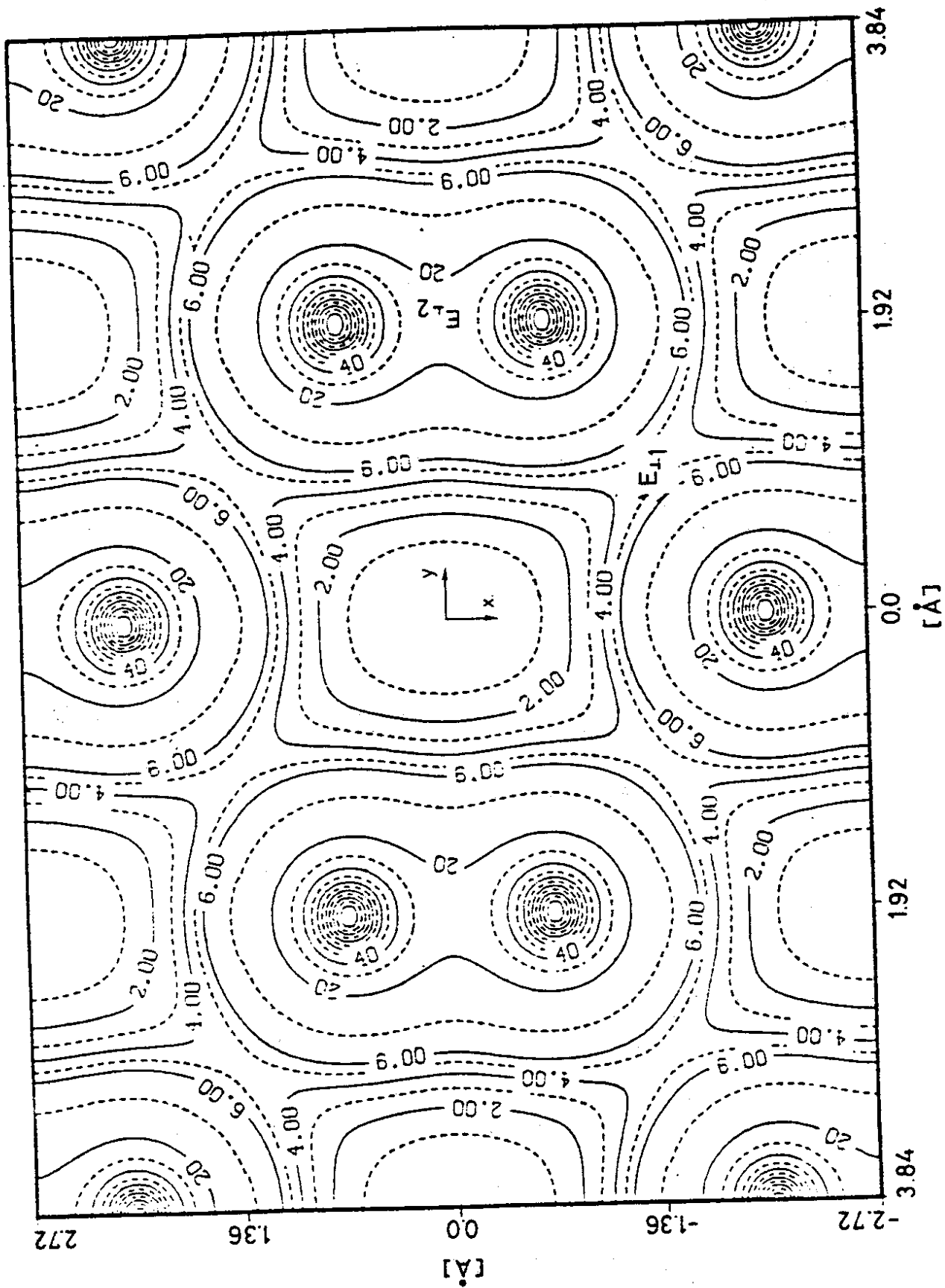


Fig. 2

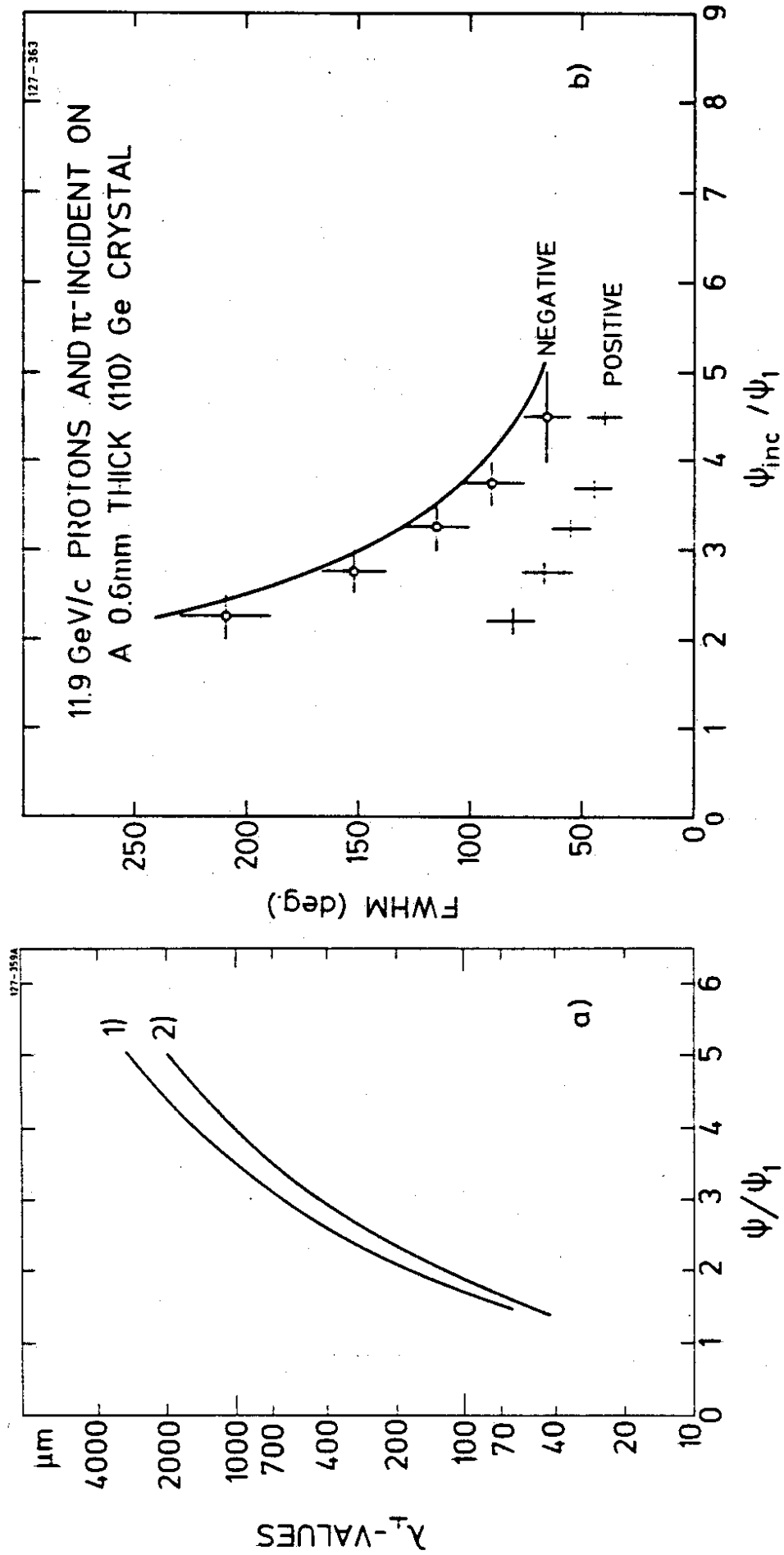


Fig. 3

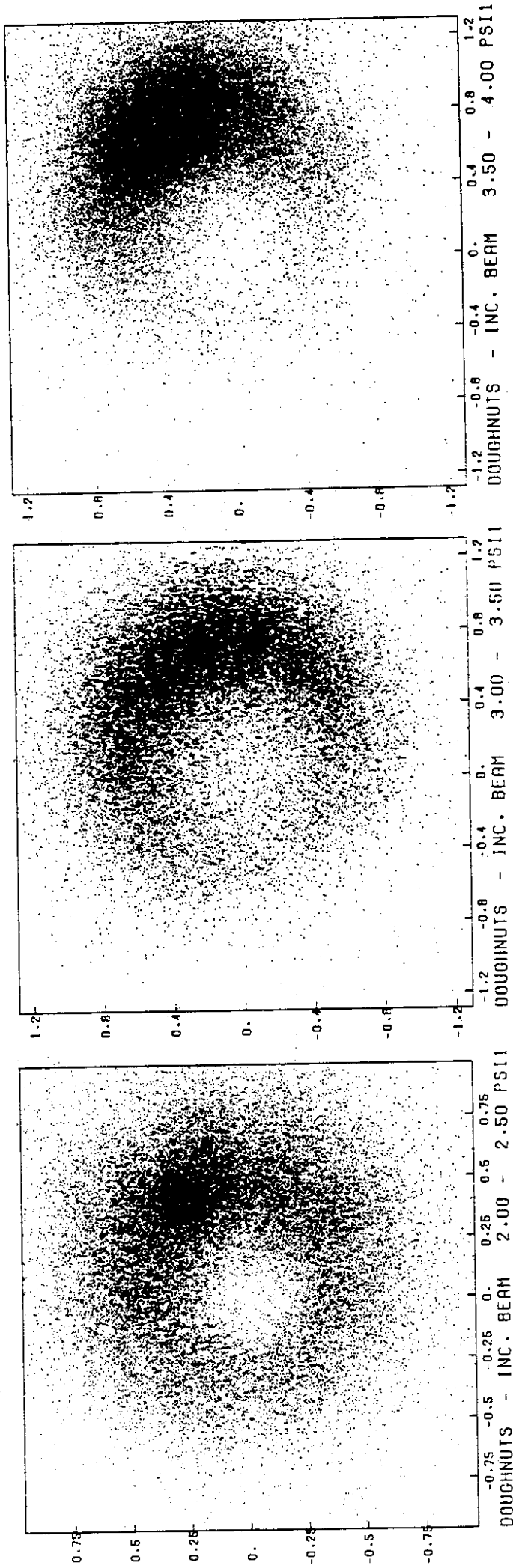


FIG. 4

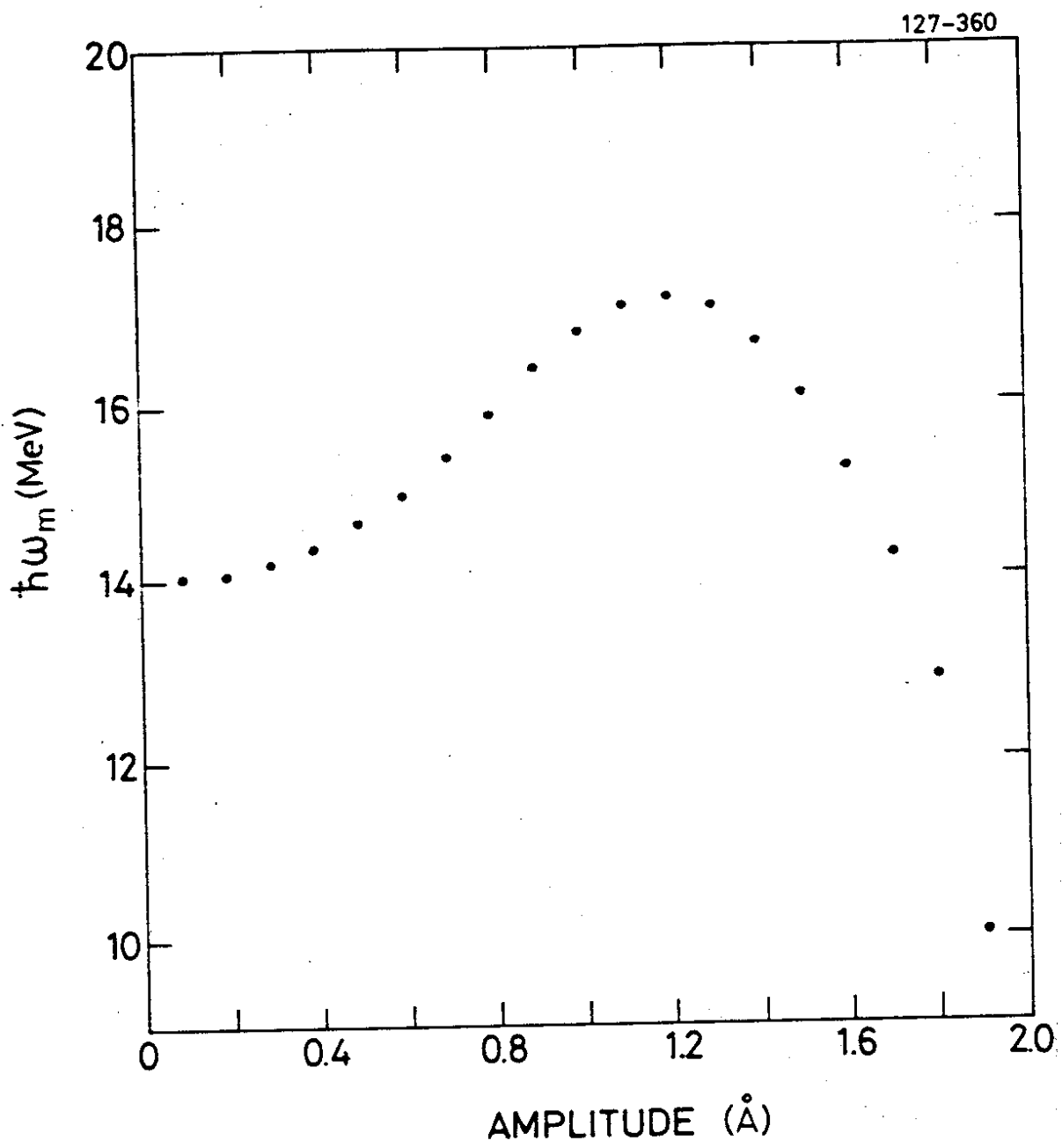


Fig. 6

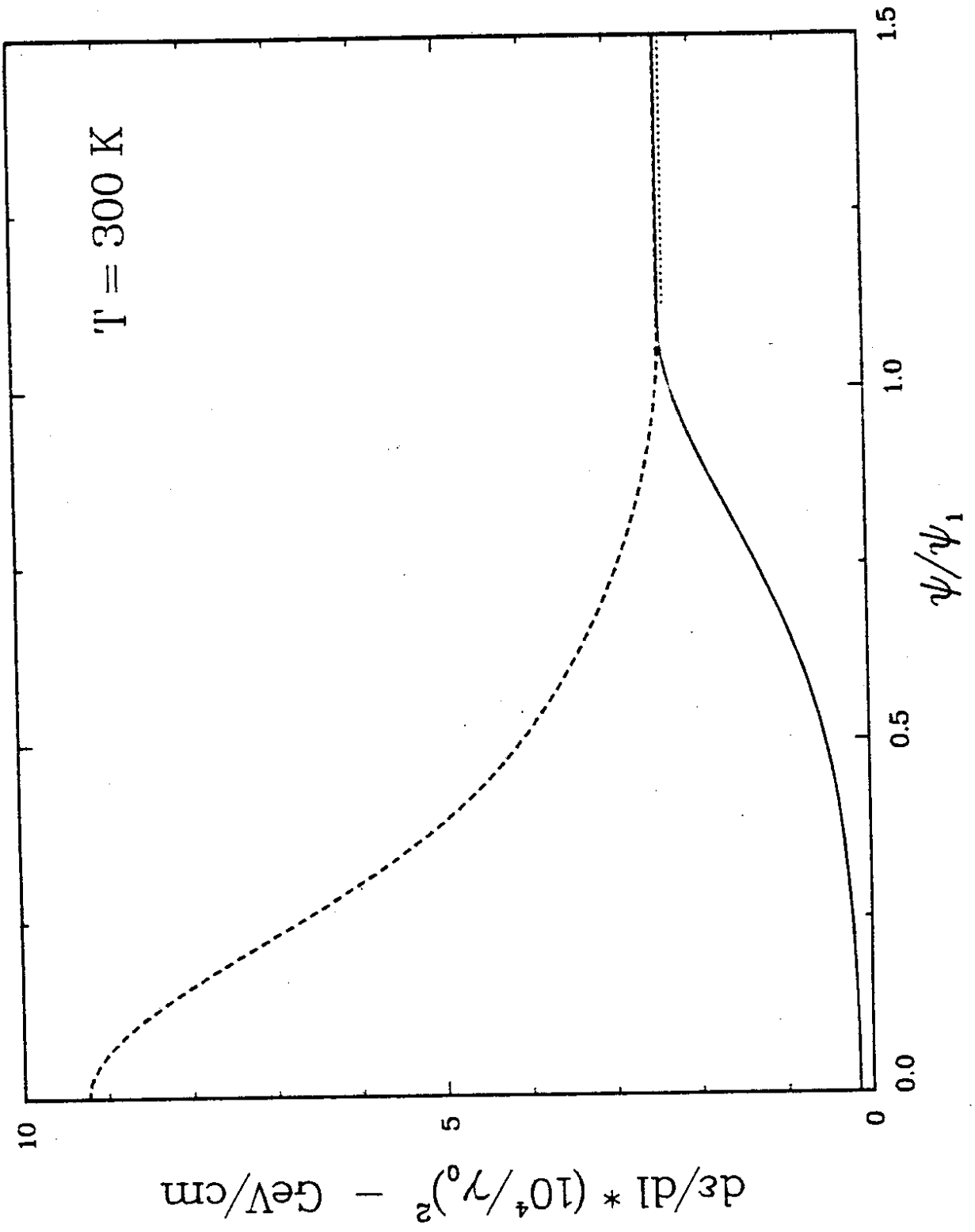


Fig. 7

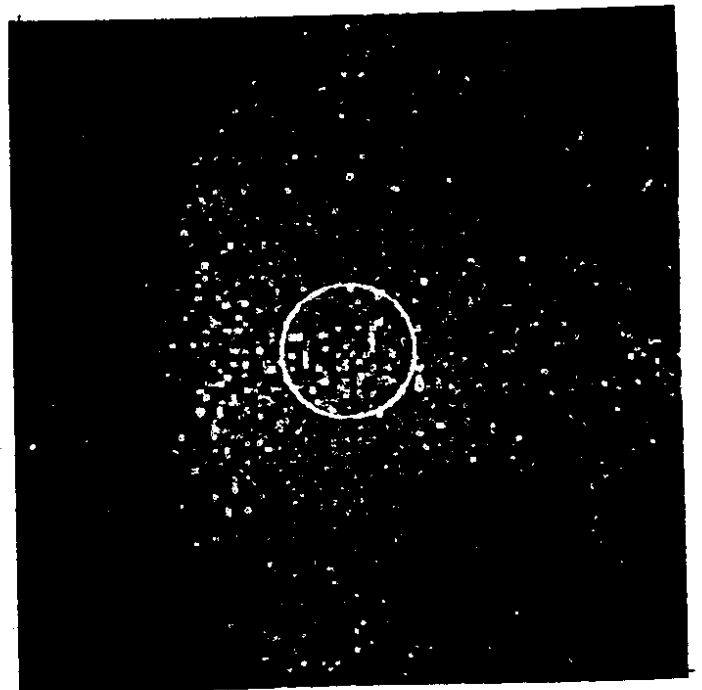
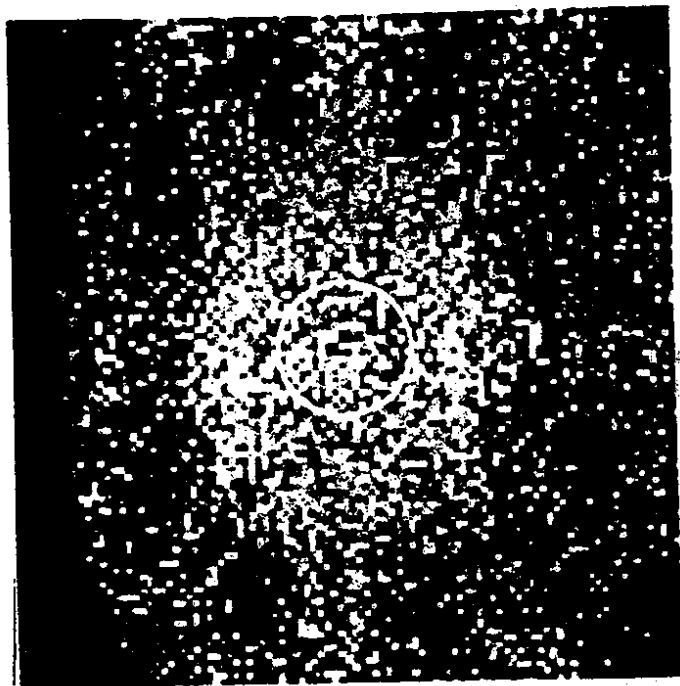
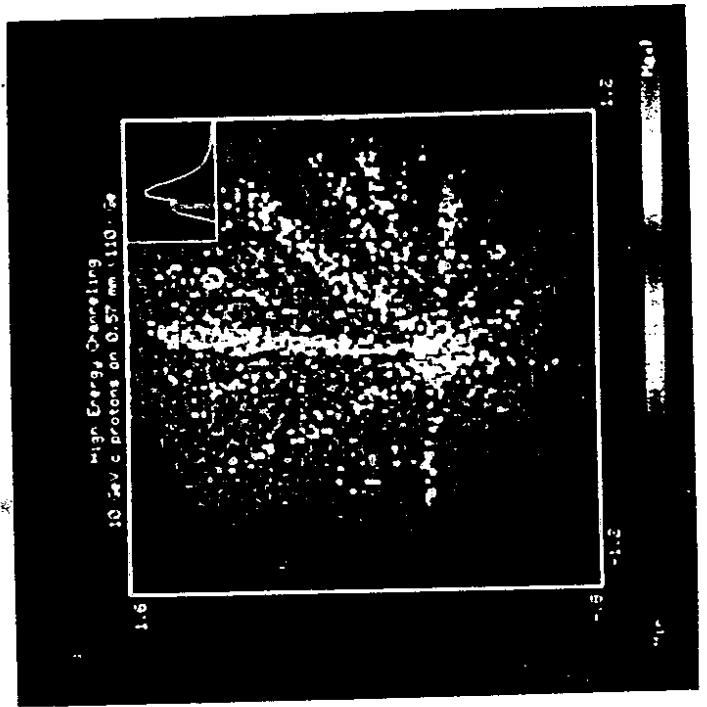
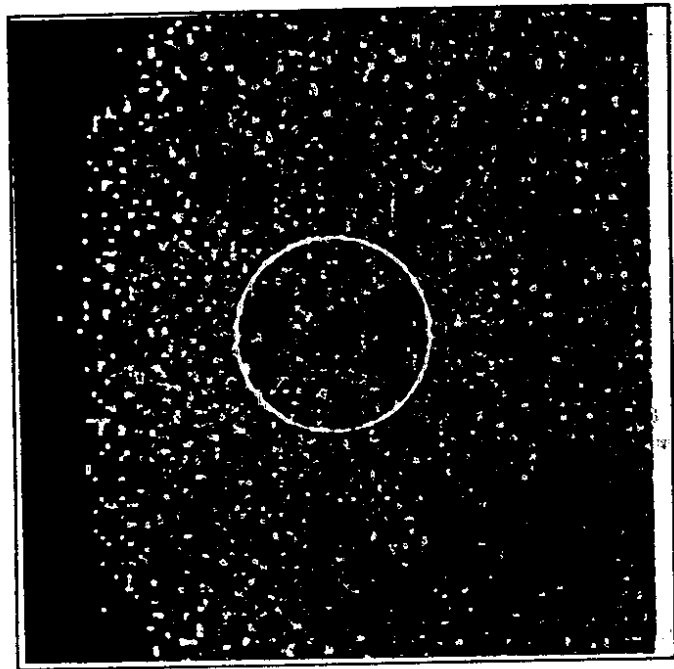


Fig. 8

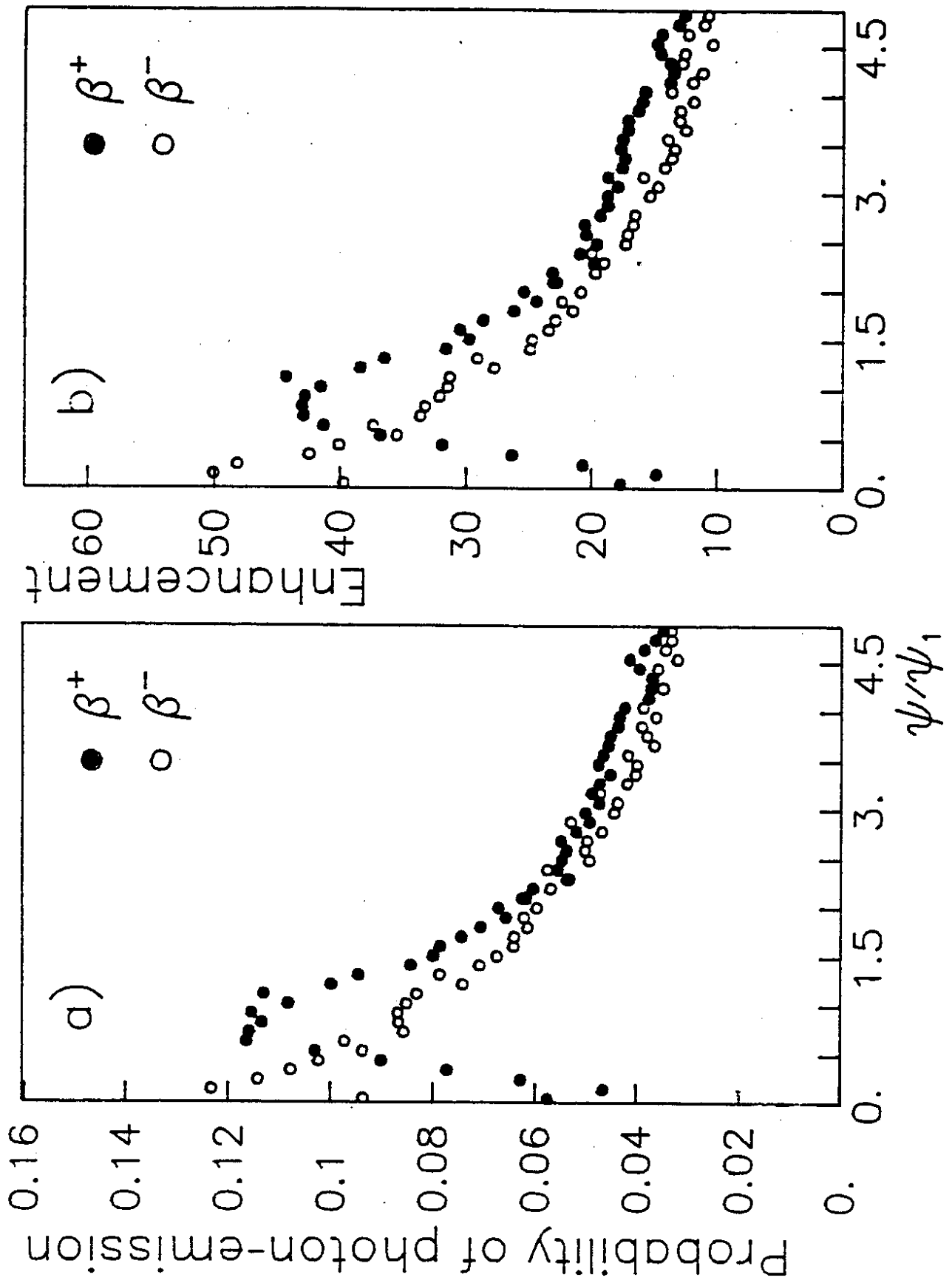


Fig. 9

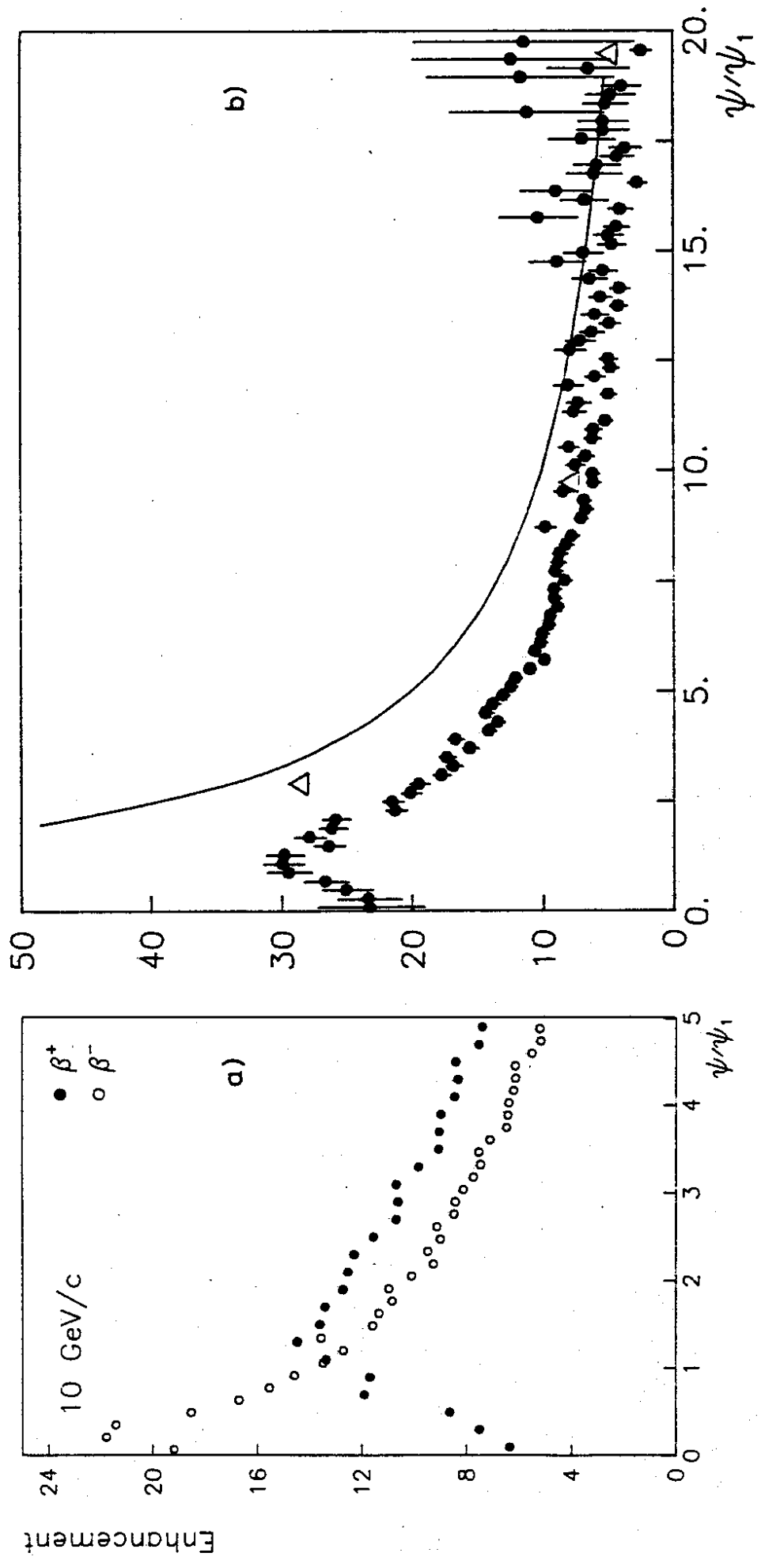
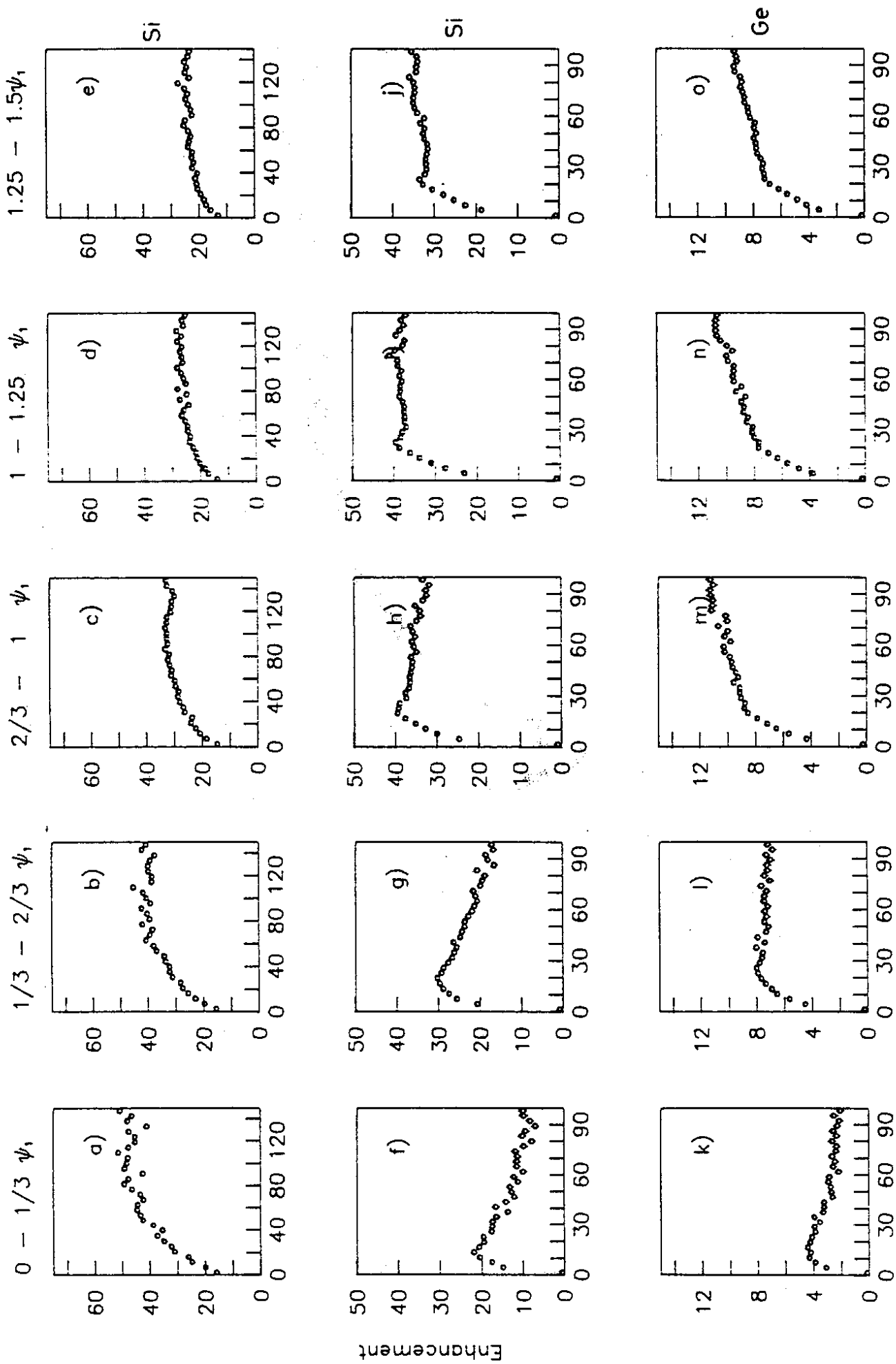


Fig. 10



E_γ (MeV)

Fig. 11

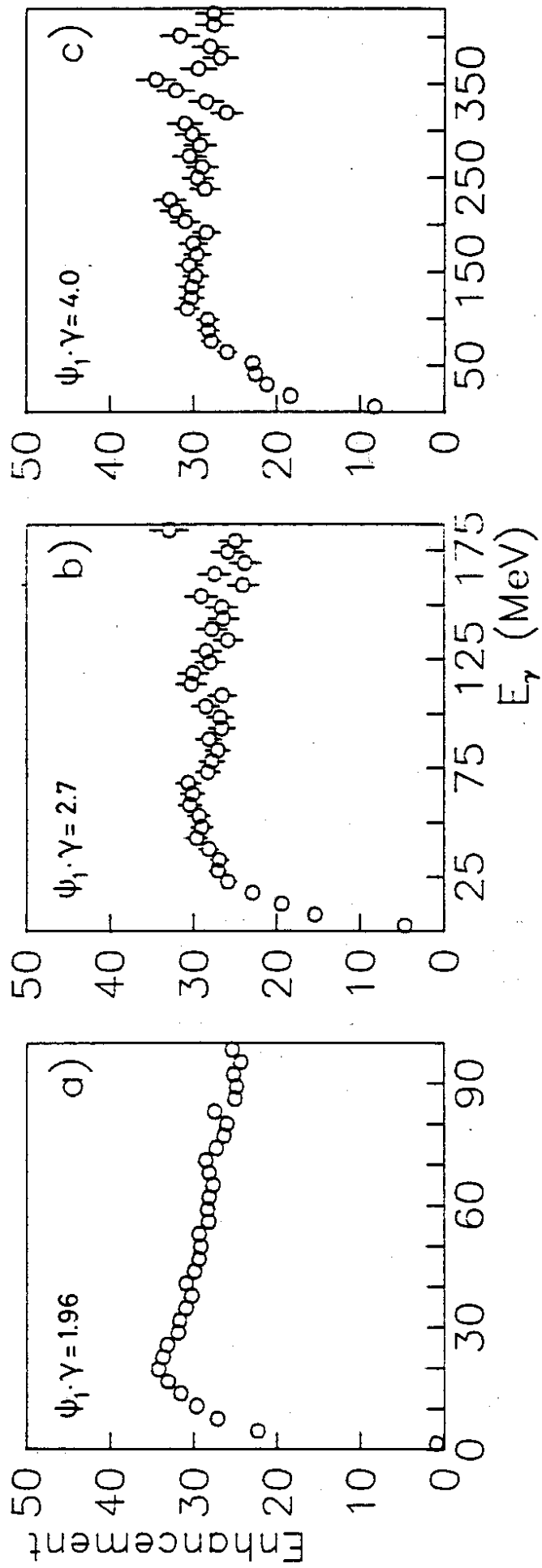


Fig. 12

10 GeV/c e^- on $\langle 110 \rangle$ Si

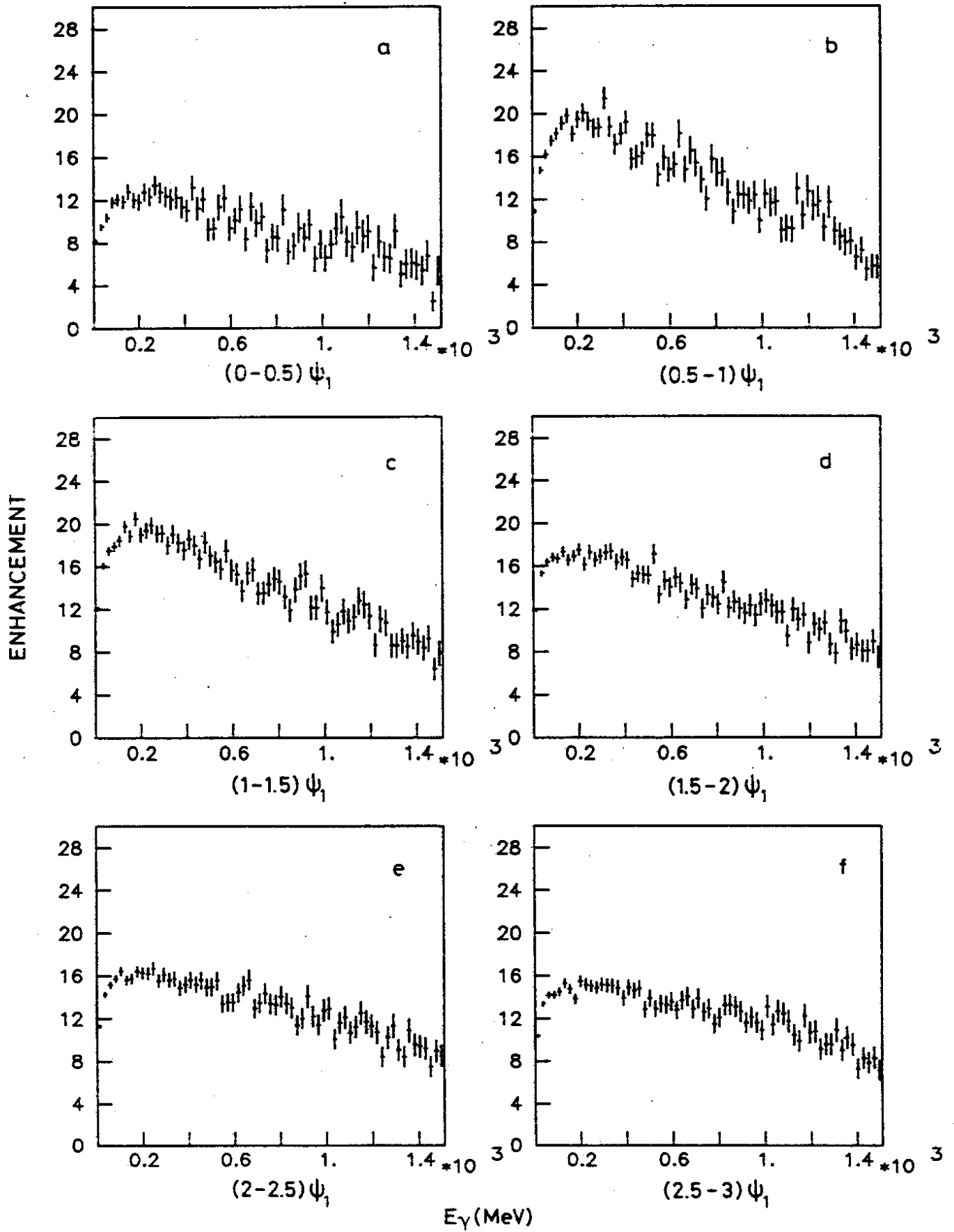


Fig. 13

10 GeV/c e^+ on $\langle 110 \rangle$ Si

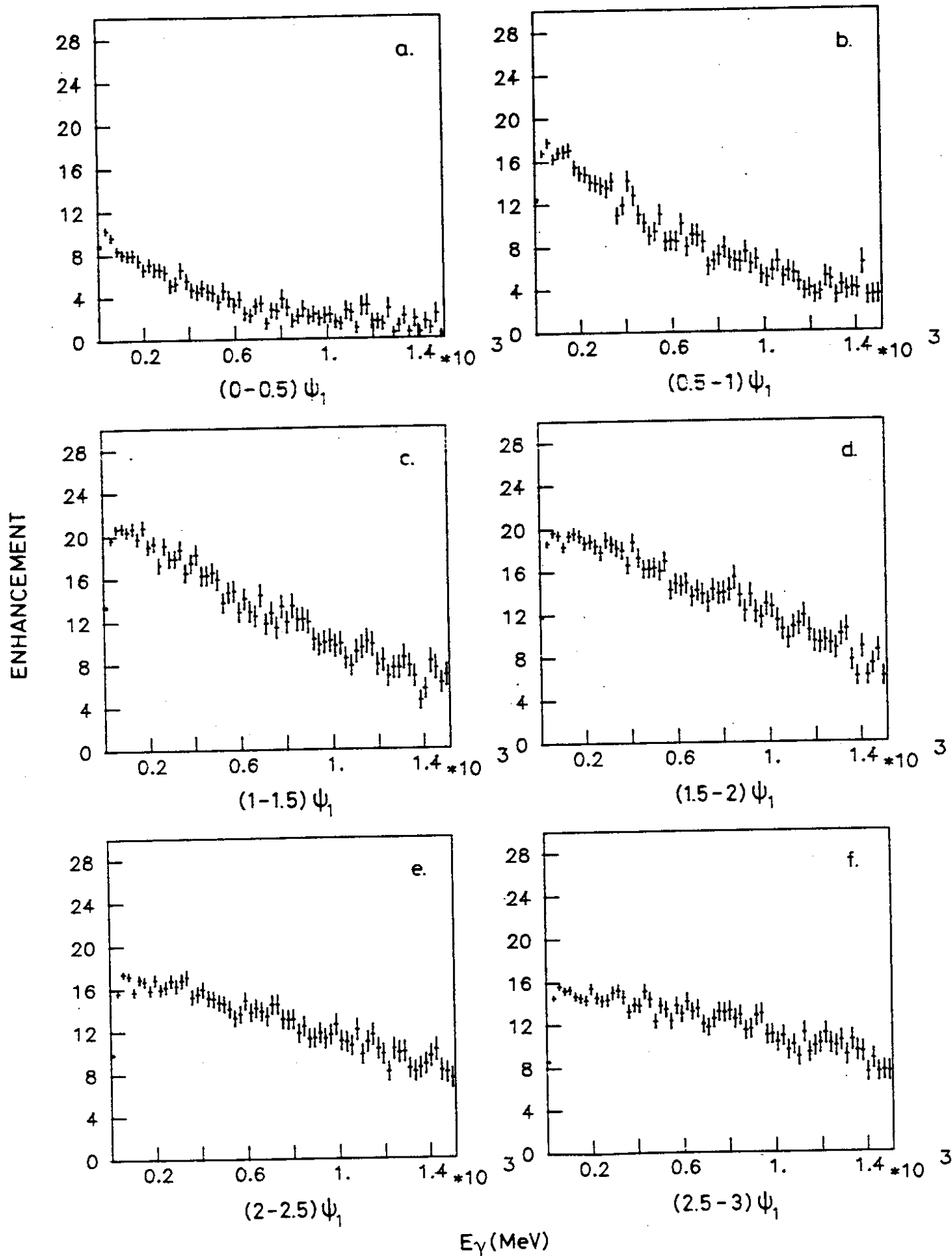


Fig. 14

20 GeV/c e^+ on $\langle 110 \rangle$ Si

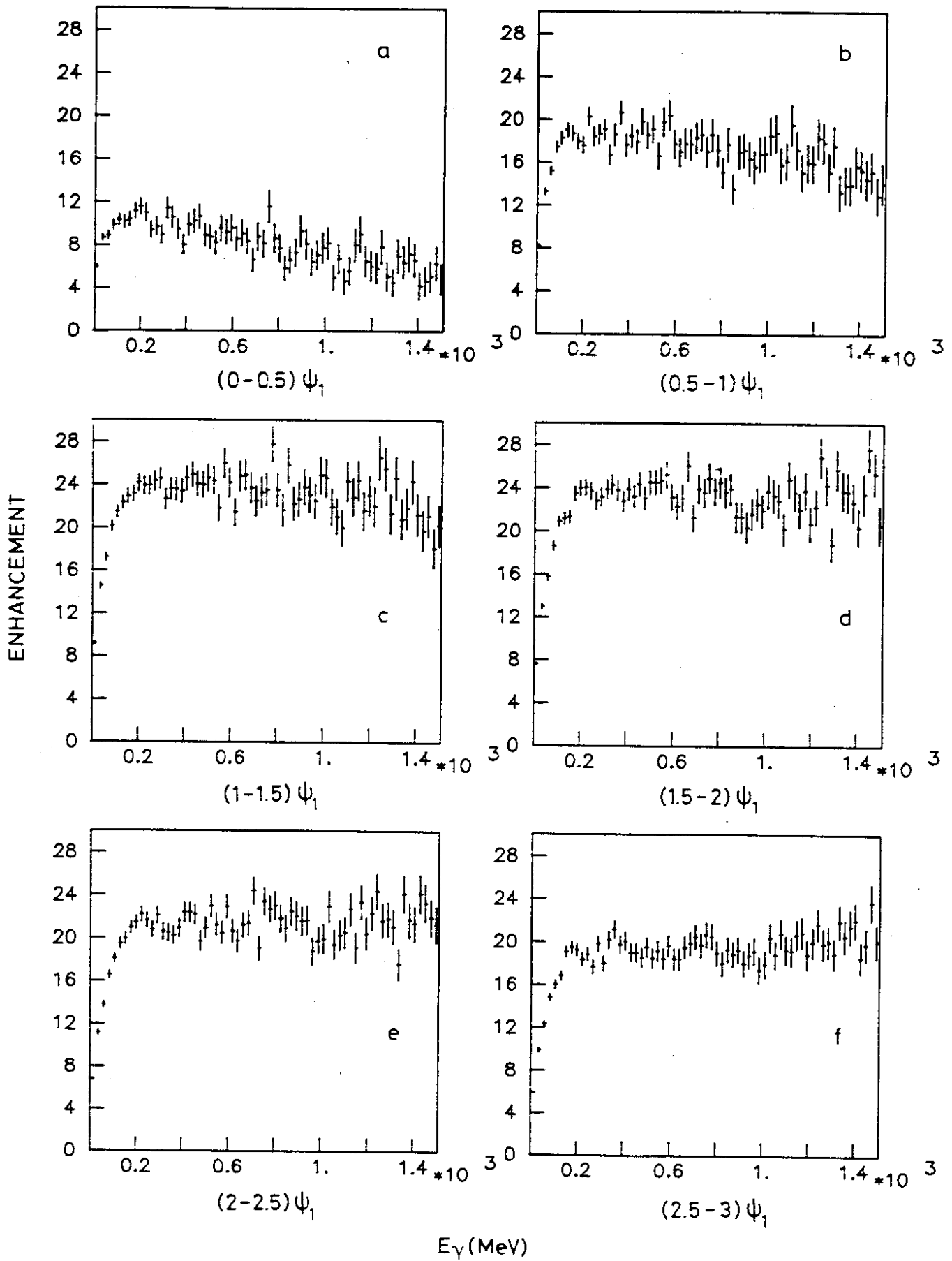


Fig. 15

20 GeV/c e^+ on $\langle 110 \rangle$ Si

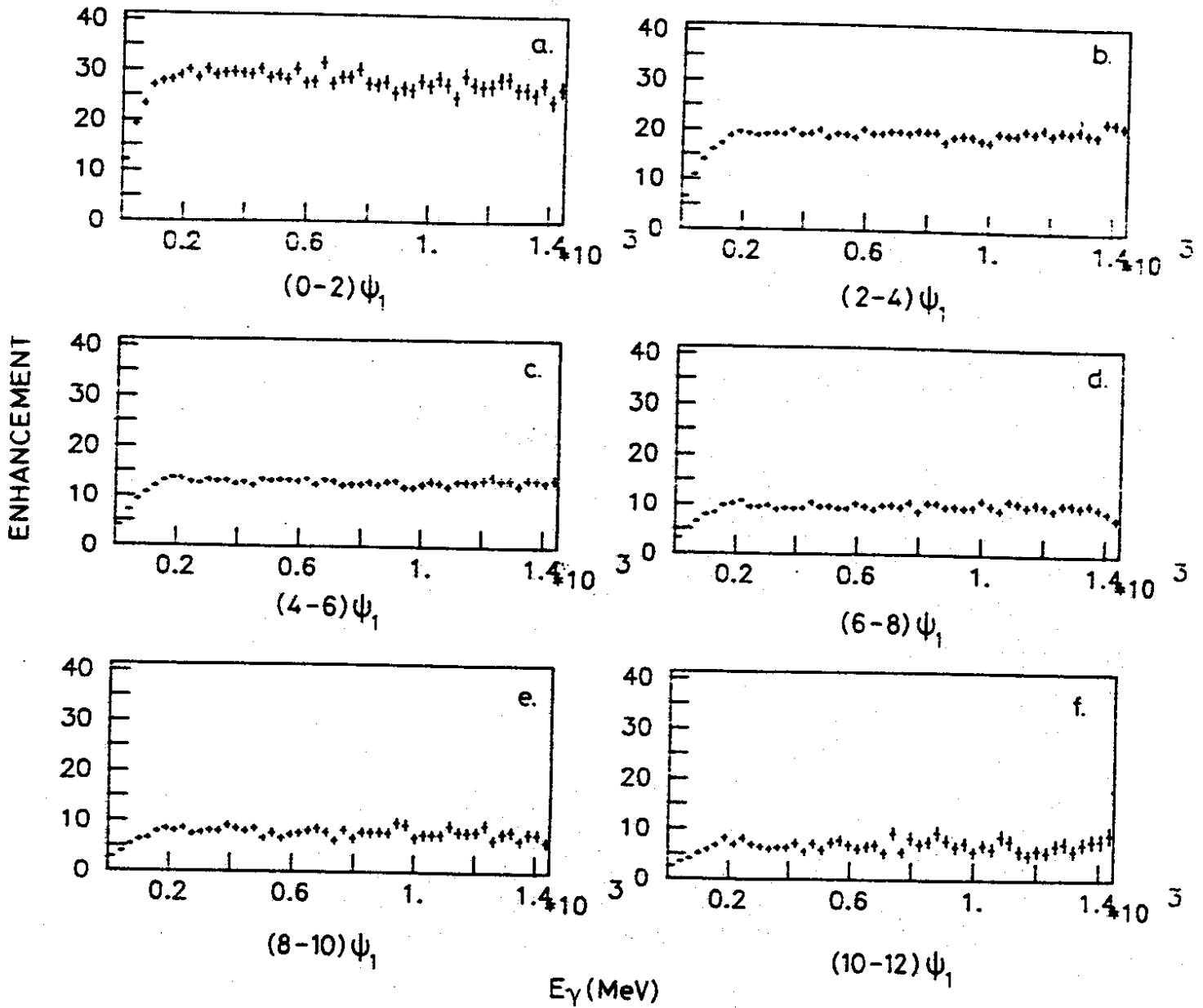


Fig. 16

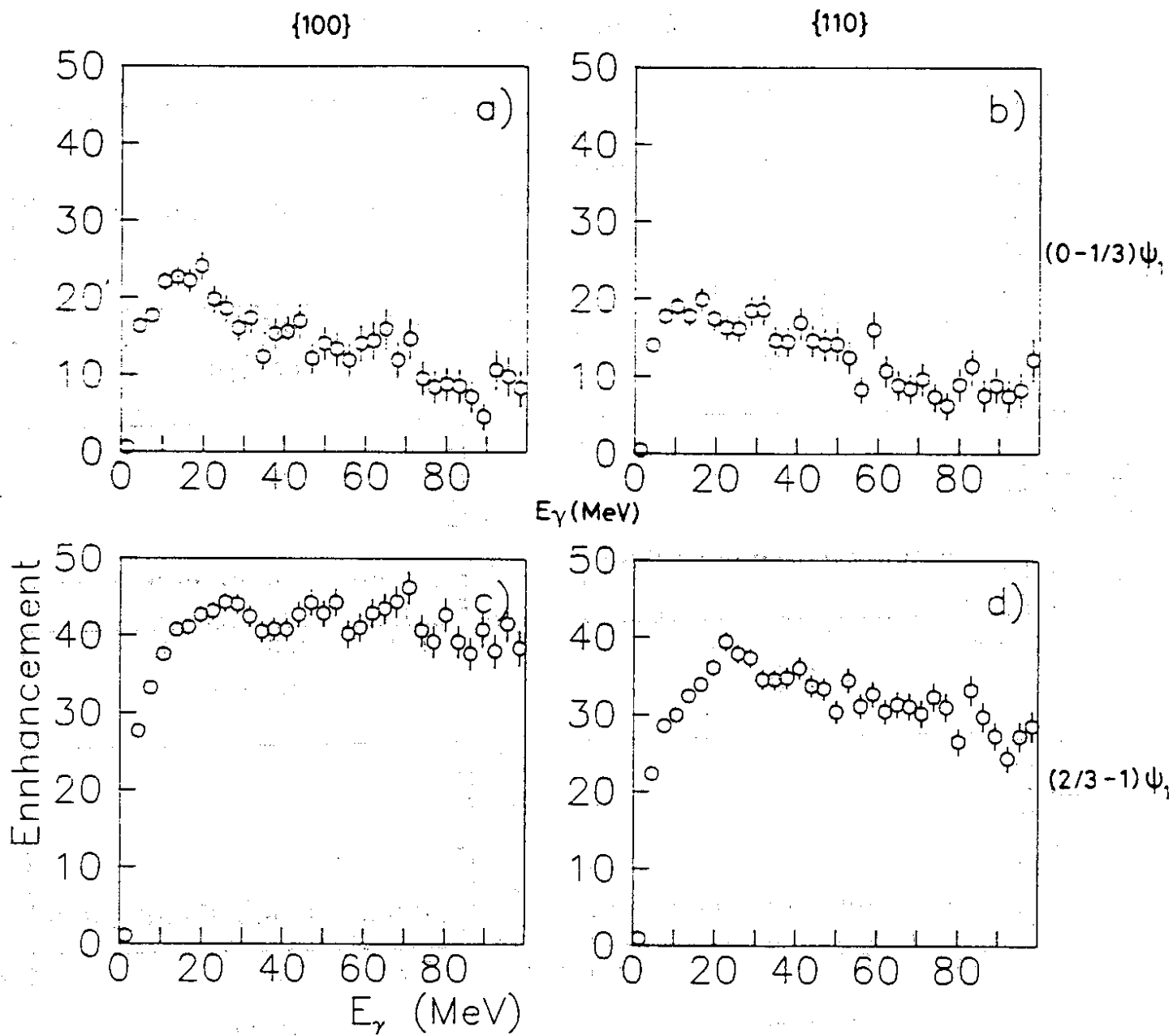


Fig.17

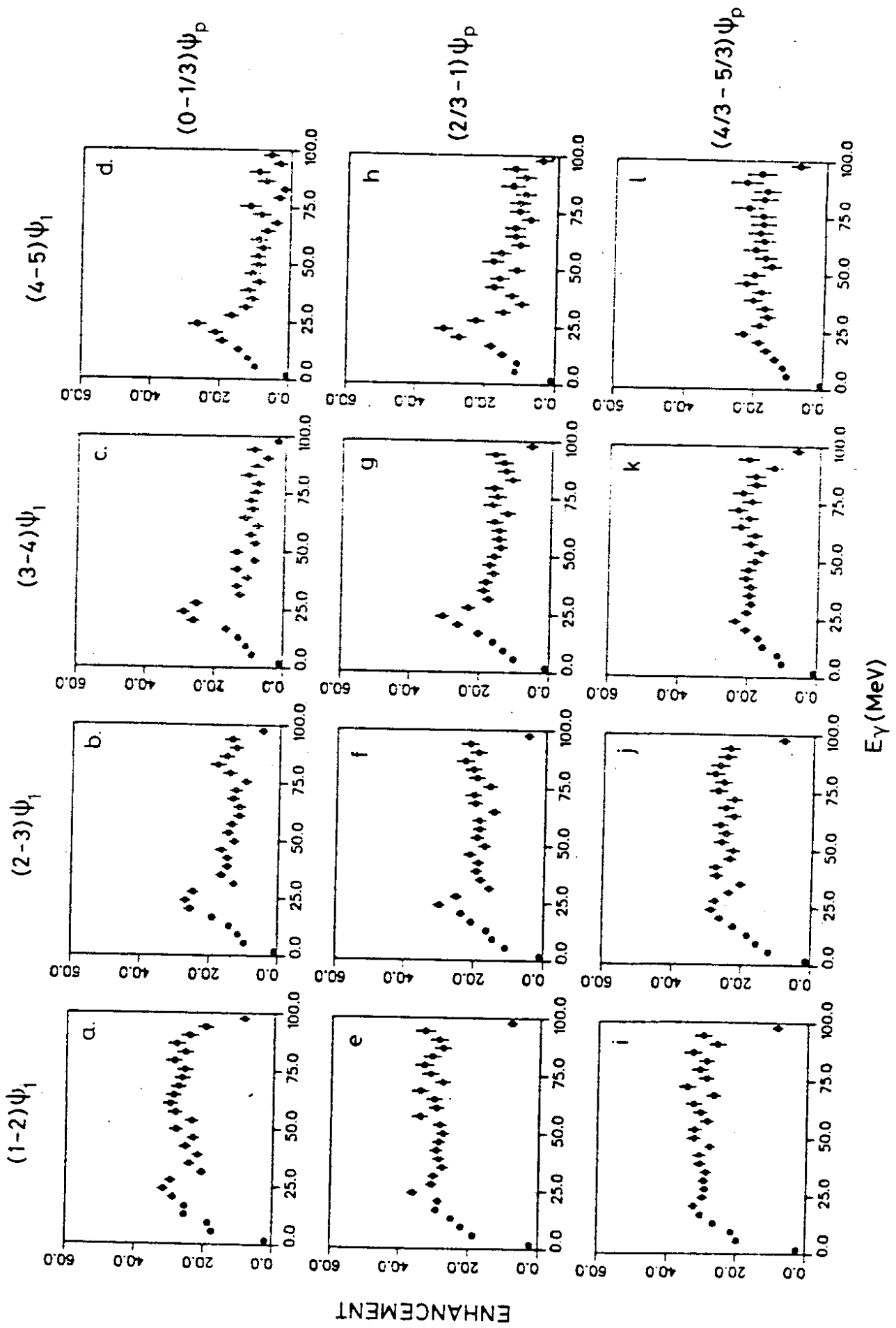


Fig. 18